

3D scanning of non-opaque objects by means of infrared imaging

Luis Alonso Sánchez Secades

Laboratoire d'Electronique, Informatique et Image

Université de Bourgogne

A Thesis Submitted for the Degree of
MSc. Erasmus Mundus in Vision and Robotics (VIBOT)

·Le Creusot, June 18, 2008·



Abstract

Sánchez Secades, L.A. 3D scanning of non-opaque objects by means of infrared imaging. 2008.

3D surface acquisition of objects is a subject which has been studied to a large extent, a significant number of techniques for acquiring shape have been proposed and a wide range of commercial solutions is available. Nevertheless, today's systems still have major difficulties when acquiring objects with non-lambertian surfaces in the visible light spectrum, as in the case of transparent, semi-transparent or very reflective materials (e.g. glass, crystals, some plastics and shiny metals).

Laser light based systems are one of the most common and accurate solutions used in industry, but for the previously mentioned materials it is more difficult to detect or trace the laser light, and it has not yet been possible to develop a fast and accurate non-contact technique. Furthermore, it has been necessary to use special coatings to cover the object's surface before a scan, or to develop more complex systems when compared to laser scanners. Some of these latter techniques are based on light polarization, conoscopic holography, dynamic lightning, reflection models, and other model minimization techniques.

This thesis presents an analysis for addressing the issues associated to visible light laser scanners. The radiative properties of materials are taken into account and an example case of analysis is developed for soda-lime glass objects. Additionally, a prototype infrared laser scanning system was developed and it is reviewed in detail. With the prototype, designed for demonstrative purposes, it was also possible to obtain reconstructions using other materials apart from glass. The system only requires a single long-wave infrared camera and an infrared laser. Its limitations are identical to those of a standard laser scanner, but it performs significantly better on non-opaque surfaces. The resulting reconstructions could also have been textured with the object's apparent temperature, since it is also measured by the camera.

Keywords: Laser scanning, 3D reconstruction, infrared imaging, non-opaque material, transparent object, reflective surface.

*Luis Alonso Sánchez Secades, Laboratoire Le2i, Université de Bourgogne.
Le Creusot, France.*

© Luis Alonso Sánchez Secades 2008.

The sky is filled with stars, invisible by day.

Henry Wadsworth Longfellow

*Genius is the ability to see things invisible, to manipulate things intangible,
to paint things that have no features.*

Joseph Joubert

*Adieu, dit le renard. Voici mon secret. Il est très simple: on ne voit bien
qu'avec le coeur. L'essentiel est invisible pour les yeux.*

Antoine de Saint-Exupery (Le Petit Prince)

Contents

Acknowledgments	iv
1 Introduction	1
1.1 Previous work	2
1.2 Thesis outline	4
2 Background	5
2.1 Radiative properties of materials	5
2.2 Example case of soda-lime glass	7
2.2.1 A model for glass laser heating	10
2.2.2 Material behavior simulation (FEA Fundamentals)	12
2.3 3D laser scanning	14
2.3.1 Laser peak detection	14
2.3.2 Camera calibration	16
2.3.3 Triangulation using the complete quadrangle technique	20
3 Solution	21
3.1 Finite Elements Analysis	21
3.2 3D infrared laser scanning	26
3.2.1 Library specifications and requirements	27
3.2.2 The complete quadrangle technique	27
4 Experimental Results and Analysis	35
4.1 Simulations	35
4.1.1 Experimental setup	35
4.1.2 Validation of the superficial heating model	35
4.2 3D reconstruction	37
4.2.1 Experimental setup	37
4.2.2 Triangulation results	38
5 Conclusions and future work	43
A Finite Elements Analysis using ELMER	45

List of Figures

1.1	Laser light triangulation system: Other patterns, such as points, can be used instead of lines and also multiple camera systems can be found. . . .	1
1.2	Samples of incorrect acquisitions using the Konica Minolta VI-910 scanner [20].	3
2.1	Behavior of light on different surfaces.	6
2.2	Response of a semi-transparent medium to electromagnetic radiation. . . .	6
2.3	Glass absorption, reflection and transmission coefficients depending on the radiation wavelength.	8
2.4	Glass transmission depending on the radiation wavelength.	9
2.5	Relative response curves for a number of IR cameras.	10
2.6	Diagram of a piece of glass irradiated by a CO2 laser beam.	12
2.7	Example of a 2D nodal network.	13
2.8	Summary of nodal finite difference equations considering 2D steady state conduction and convection.	15
2.9	Laser peak and first derivative.	16
2.10	Cross-ratio of a pencil of lines.	17
2.11	The complete quadrangle.	18
2.12	Determination of 2D-3D correspondences using the complete quadrangle. . . .	19
3.1	Sample of glass	22
3.2	Geometry definition	22
3.3	3D mesh generation for FEA	23
3.4	3D mesh generation for FEA	25
3.5	Diagram of the prototype laser scanning system.	26
3.6	Positioning of the complete quadrangle at different known depths	28
3.7	Enhancement of the complete quadrangle calibration images.	29
3.8	CQCornersWidget calibration interface.	30
3.9	Computation of additional correspondence points.	31
3.10	Ransac fitting of the laser line during the system calibration.	32
3.11	Laser peak estimation for triangulation of 3D points.	34
4.1	Experimental setup for validating the superficial laser heating model. . . .	35
4.2	Validation results for the superficial laser heating model.	36
4.3	Experimental setup for 3D surface surface acquisition.	37

4.4	Complete quadrangle in glass.	38
4.5	Example of an input image sequence.	39
4.6	Triangulation results for a wine glass.	40
4.7	Accuracy of the point clouds.	41

List of Tables

2.1	Summary of some thermal properties of soda-lime glass and air	10
4.1	Comparison of values measured directly using a caliper and using the triangulated points	42

Acknowledgments

I would like to thank all the people that made this thesis possible, the staff from all the three institutions associated to the Master's VIBOT, and also my many student colleagues for these two years in which we worked hard, learned and grew together.

I wish to thank my supervisor, Prof. Fabrice MERIAUDEAU, for providing me the opportunity of exploring alternative imaging techniques, for believing in my work and for always offering his support at all levels. I am also grateful to Prof. David FOFI and Prof. Joaquim SALVI, who were always available for providing their assistance.

After this amazing experience, I can only recognize that I would have been lost without your help.

Lastly, and most importantly, I wish to thank my parents, Patricia SECADES and Héctor SANCHEZ, and my family. All of this would have been impossible without your love and dedication. To them I dedicate this thesis.

Chapter 1

Introduction

Today, 3D surface acquisition is a common task carried out by the industrial, medical, military and general consumer sectors. From volumetric representations of real world objects, it is possible to carry out quality control tasks, solve inverse engineering problems, find optimal paths for robots and to create animation models, among many other emerging activities.

The most common acquisition systems would probably be those based on laser light triangulation (Figure 4.6), in which a camera is used to study the laser pattern deformation, allowing to determine the depth of points in the pattern. The laser pattern projection leads to a simplification of the correspondence problem (i.e. finding a set of corresponding points, or “correspondences”, given a set of images of a 3D scene), in order to obtain dense reconstructions.

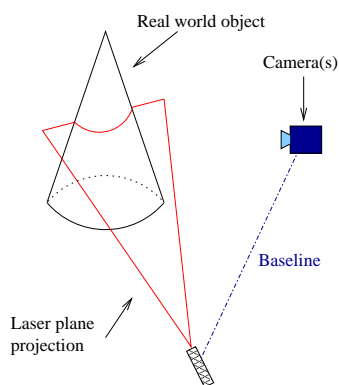


Figure 1.1: Laser light triangulation system: Other patterns, such as points, can be used instead of lines and also multiple camera systems can be found.

Nevertheless, this type of systems cannot be used when the objects to be acquired are transparent, semi-transparent or very reflective. In these cases the laser light might travel through the object or it can also be reflected in such a way that it is not captured by a camera. This behavior leads to increasing the complexity of finding 2D-3D

correspondences. Figure 1.2 illustrates how a commercial scanner fails when acquiring some objects.

This thesis presents an analysis for addressing the issues associated to the behavior of visible light on non-opaque materials. By studying the radiative properties of materials and developing an example analysis case for soda-lime glass objects, it is shown that laser scanners can be adapted to work with non-opaque materials. A prototype infrared laser scanning system is presented for demonstrative purposes. The system only requires a single long-wave infrared camera and an infrared laser. Its limitations are identical to those of a standard laser scanner, but it performs significantly better on non-opaque surfaces and the resulting reconstructions can also be textured with the object's apparent temperature, since it is also measured by the camera.

1.1 Previous work

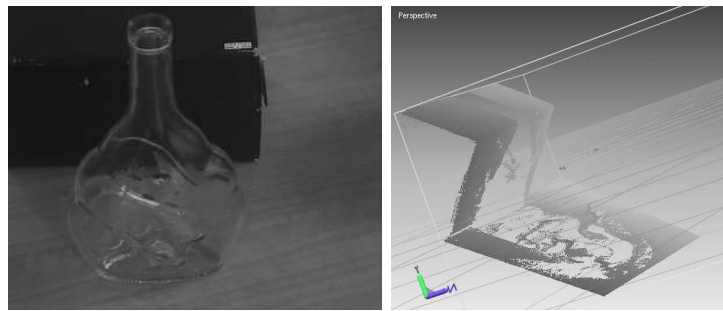
Until today, when trying to acquire non-opaque objects it has been necessary to use special coatings to cover the object's surface before a scan, or to use more complex systems when compared to laser scanners. In general, it is only recently that some prospective techniques for modeling transparent surfaces have appeared.

For instance, in the computer graphics community Goesele, Lensch et al. [3] proposed a method for determining the scattering behavior of translucent objects by using a laser, but the geometry was initially acquired by covering the object with a white coating. Similarly, Matusik, Pfister et al. [5] presented an acquisition and rendering system for transparent and refractive objects from arbitrary viewpoints using a novel illumination, but the recovered geometry is just the visual hull (i.e. a very rough approximation of the object's shape).

In fact, only few works address the problem of directly recovering the object's shape. Kutulakos et al. [17] develop a theory for recovering the 3D shape of refractive and specular objects by light-path triangulation, being able to recover the shape of some diamonds. Bonfort et al. [26] and Fanany et al. [19] propose similar geometric methods. Hasinoff and Kutulakos [11] have also proposed a way for reconstructing 3D models of semitransparent scenes such as fire.

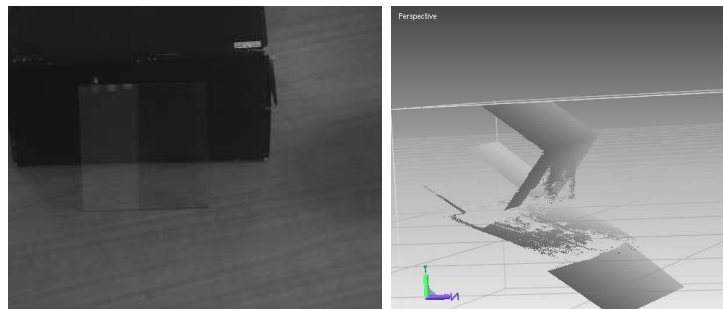
At the laboratory Le2i, in which this thesis was carried out, polarization imaging and active lighting was successfully used for reconstructing specular metallic surfaces [4]. Currently, the possibility of using similar light polarization techniques is being studied for the case of transparent objects. Finally, conoscopic holography systems [10] have also proved to be useful for some cases where triangulation methods failed.

One major disadvantage is that most of the previous approaches require to know in advance the specific type of object or material to be modeled (e.g. transparent, semi-transparent, specular), and most approaches work for only one of these types of objects. In the present work, this constraint is softened, and solely triangulation principles are used for acquiring the shape. As a result, this system should operate faster than those based on light polarization, conoscopic holography, dynamic lighting, reflection models or other model minimization techniques, specially when acquiring the surface of medium sized objects.



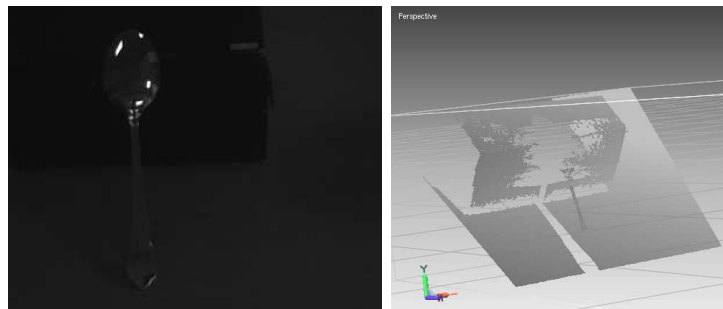
(a) Glass bottle.

(b) Bottle reconstruction.



(c) Piece of window glass.

(d) Glass piece reconstruction.



(e) Stainless steel spoon.

(f) Spoon reconstruction.



(g) Experimental setup

Figure 1.2: Samples of incorrect acquisitions using the Konica Minolta VI-910 scanner [20].

1.2 Thesis outline

This thesis is structured in four more chapters.

In Chapter 2, the radiative properties of materials will be introduced. In order to understand how it is possible to laser scan non-opaque surfaces, an example case of glass objects will be developed. Towards the end of the chapter, the principles of laser scanning will be also presented.

Chapter 3 focuses on the proposed solution, defining the system specifications and the algorithms used for simulating the material behavior and for 3D laser triangulation.

In Chapter 4, the different experimental setups are reviewed. Subsequently, the obtained results are presented and analyzed. Some observations for improving the system's performance are taken into account.

Finally, in Chapter 5 the conclusions of the thesis are presented and the areas in which future efforts should focus are explored.

Chapter 2

Background

When the literature refers to non-opaque materials or non-lambertian surfaces, it usually means that the material properties allow visible light to pass through or that the light is reflected in a particular way (Figure 2.1). Nonetheless, the electromagnetic radiation outside the visible spectrum also interacts with matter in a behavior that could be described as a combination of transmission, reflection and absorption of energy (Figure 2.2). For example, flesh is transparent to X-rays, while bone is not, making X-ray imaging useful for medicine.

In order of decreasing wavelength, some types of electromagnetic radiation are: radio waves, microwaves, terahertz radiation, infrared radiation, visible light, ultraviolet radiation, X-rays and gamma rays.

As in the case of X-rays, by studying the radiative properties of materials it is possible to adapt different shape acquisition techniques in order to work with surfaces which are normally impossible to scan using visible light sources. A special case, using infrared imaging, will be studied in the following sections.

2.1 Radiative properties of materials

Figure 2.2 illustrates three possible responses of a semi-transparent medium to irradiation. Without having to enter into details, from the heat transfer theory it is possible to establish a radiation balance, where the irradiation equals the sum of the reflection, absorption and transmission terms (for more information the reader could refer to any heat transfer or thermodynamics textbook [12]):

$$G_{\lambda} = G_{\lambda,refl} + G_{\lambda,abs} + G_{\lambda,trans} \quad (2.1)$$

In order to quantify the amount of irradiation being absorbed, reflected and transmitted, different coefficients have been defined (i.e. α , ρ and τ , respectively). In the most general case and assuming negligible temperature dependence, these coefficients depend on the angle of incidence θ and on the radiation wavelength λ . Then, for a particular medium the following balance can be derived:

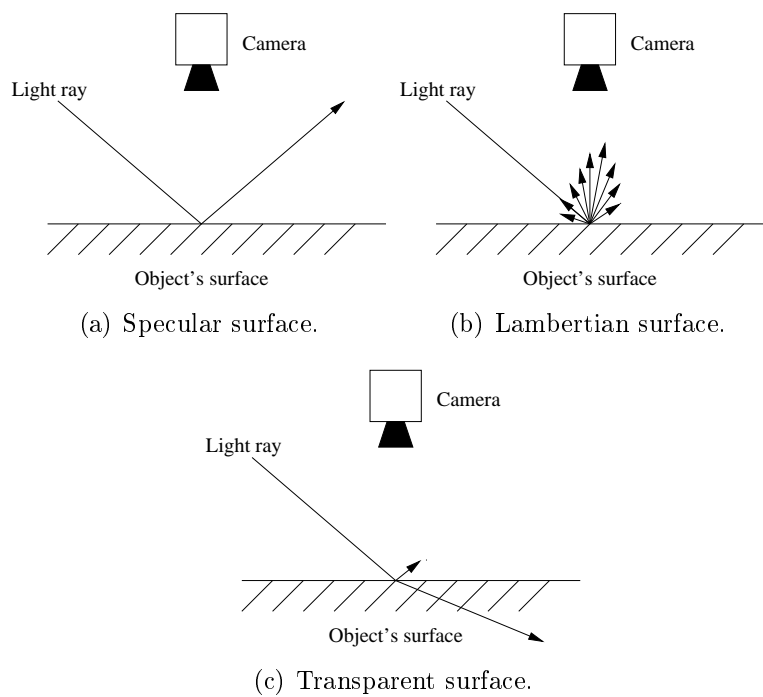


Figure 2.1: Behavior of light on different surfaces.

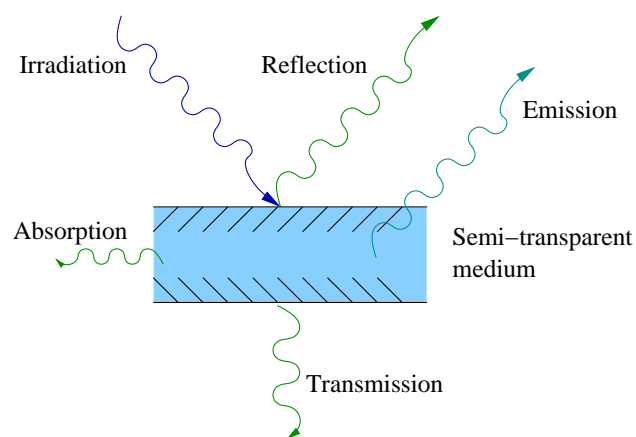


Figure 2.2: Response of a semi-transparent medium to electromagnetic radiation.

$$\alpha_{\theta,\lambda} + \rho_{\theta,\lambda} + \tau_{\theta,\lambda} = 1 \quad (2.2)$$

Finally, Kirchoff's law equates the following spectral directional properties:

$$\alpha_{\theta,\lambda} = \epsilon_{\theta,\lambda} \quad (2.3)$$

, where ϵ is the surface emissivity. It is only a contrast between the emission of a particular body and the ideal behavior of a black body at the same temperature.

Having stated this principles, we can proceed to analyze a sample case of a material which is difficult to scan using visible light, as is the case of common glass. Also notice that until this point, materials were not studied at a microscopic level. Details such as surface roughness were not considered and, if this was the case, some other techniques would be more useful for the analysis (e.g. speckle methods).

2.2 Example case of soda-lime glass

Since it has been mentioned that different materials have different absorption, radiation and transmission coefficients, it would be interesting to study how these coefficients vary in a particular medium depending on the radiation wavelength λ . Figures 2.3 and 2.4 present some information for soda-lime glass, which is the most common variety of glass used in bottles, jars, other glass containers and windows.

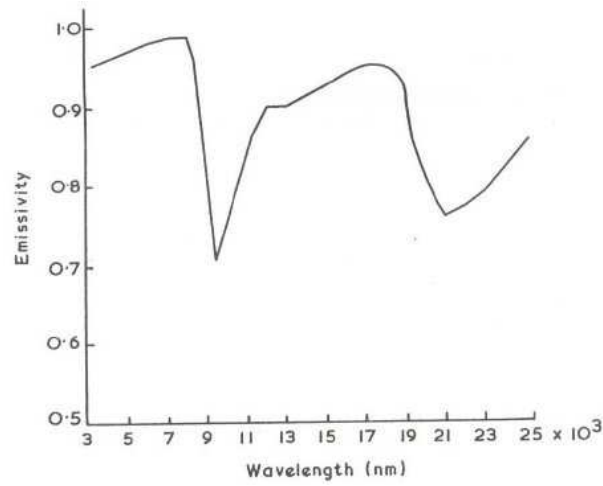
From the curves it should be noticed that at wavelengths over $5\mu m$, glass is no longer transparent and, on the contrary, presents a behavior which is a combination of reflection and absorption.

In general, most materials absorb radiations with wavelengths over $5\mu m$ and this results into an increase in temperature. For this purpose, a particular type of laser sources has a low cost and is easily available: Carbon dioxide (CO₂) lasers commonly operate at $10.6\mu m$ wavelength and can be found in a wide range of optical powers, from a few milliwatts and up to hundreds of watts. For this reason, a CO₂ laser was used for prototyping purposes. If some other specific wavelength is considered to be optimal (e.g. in the range of 3 to $5\mu m$), most laser manufacturers can provide custom, but more expensive, solutions.

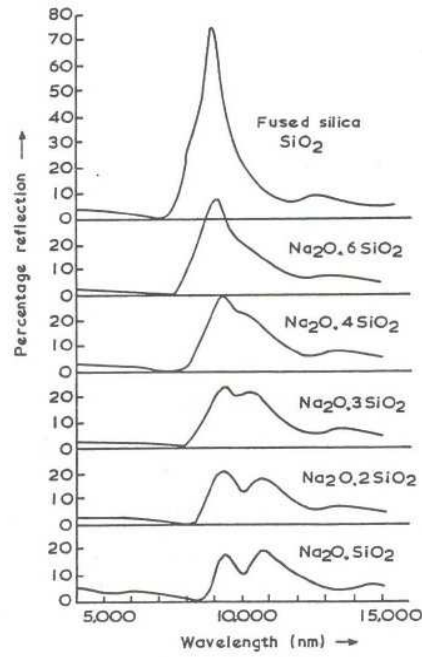
For the available laser source, long-wave infrared cameras are ideal imaging devices, since this type of sensors work in the range between 7 and $14\mu m$ wavelength. Figure 2.5 shows the response curve of some sensor technologies. Unfortunately, at $10.6\mu m$ glass is still reflective and this could be dangerous for the imaging sensor (Figure 2.3.b). Because this devices are very sensitive, some medium power reflections could reach it and produce irreparable damages. Therefore, this must be taken into account during the scanning process.

After having chosen the working wavelength, some of the thermal properties that will be useful for studying the behavior of soda-lime glass are summarized in Table 2.1.

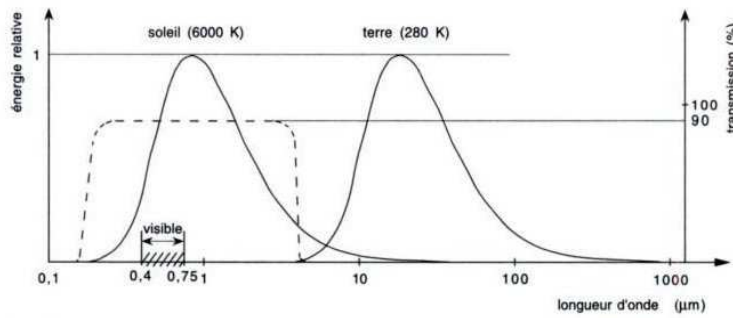
In order to know more about the material behavior when it is exposed to these type of infrared radiations, a radiative heating model could be easily developed for any type



(a) Glass emissivity depending on the radiation wavelength.

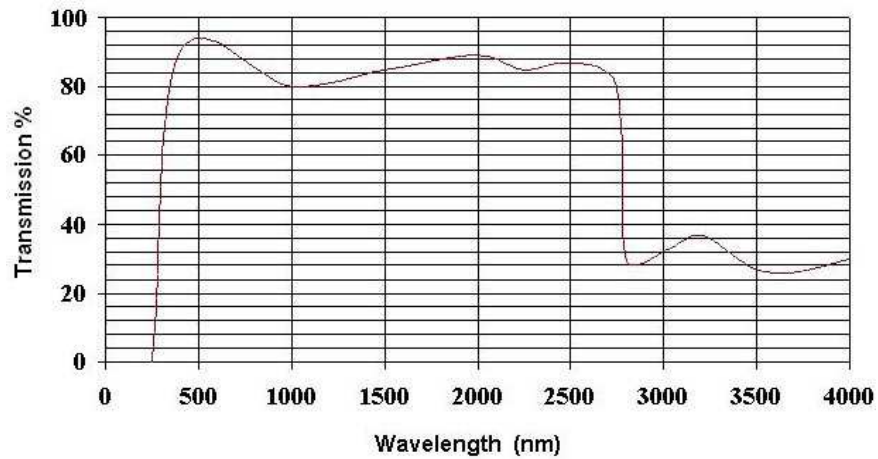


(b) Glass reflectivity depending on the radiation wavelength.

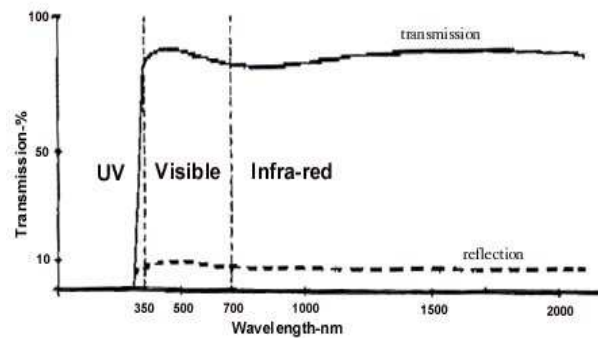


(c) Glass transmission (- - -) with respect to visible light, solar radiation and terrestrial radiation

Figure 2.3: Glass absorption, reflection and transmission coefficients depending on the radiation wavelength.



(a) Transmission curve of soda-lime glass.



(b) Glass transmission and reflection in the visible and near infrared spectrum.

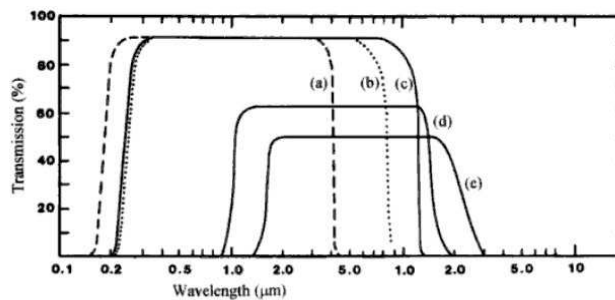


Fig. 1.9. Optical transmission curves of representative oxide, fluoride and chalcogenide glasses. (a) Silica glass, (b) $57\text{HF}_4\text{-}36\text{BaF}_2\text{-}3\text{LaF}_3\text{-}4\text{AlF}_3$ (mol%) glass; (c) $19\text{BaF}_2\text{-}27\text{ZnF}_2\text{-}27\text{LuF}_3\text{-}27\text{ThF}_4$ (mol%) glass; (d) As_2Se_3 glass; (e) $10\text{Ge-}50\text{As-}40\text{Te}$ (atom%) glass. [Reprinted from M. G. Drexage, *Treatise on Materials Science and Technology*, Vol. 26, Glass IV (Academic Press, Inc., 1985) p. 151, copyright (1985) with permission from Academic Press, Inc.]

(c) Transmission curves for other types of glass

Figure 2.4: Glass transmission depending on the radiation wavelength.

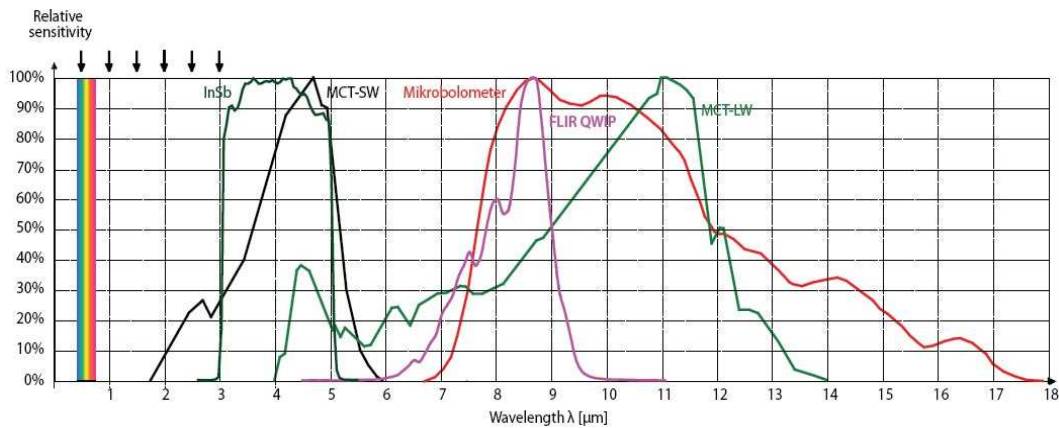


Figure 2.5: Relative response curves for a number of IR cameras.

Property name	Value	Units
Thermal conductivity	0.96, . . . , 1.10	$W/(mK)$
Specific heat capacity c	0.84	$kJ/(kgK)$
Density ρ	2400, . . . , 2800	kg/m^3
Emissivity ϵ	0.75, . . . , 0.92	–
Thermal conductivity of air (20°C)	0.03	$W/(mK)$
Convection heat transfer coefficient with air	10, . . . , 100	$W/(m^2K)$
Glass transition temperature	over 833	K
Critical tension stress	70	MPa

Table 2.1: Summary of some thermal properties of soda-lime glass and air

of material. The next section will introduce such type of modeling and the reasons why this step is very useful for developing a prototype infrared laser scanning system.

2.2.1 A model for glass laser heating

It has been mentioned that reflected laser light rays could easily damage the imaging sensor. For this thesis, an infrared camera based on uncooled microbolometer technology, i.e. a FLIR Thermacam S40, was available for the experiments. This camera can be particularly affected and destroyed by direct irradiation, as it was evidenced by previous experiments from other students.

In order to acquire image sequences where the heating pattern produced by the laser is enhanced, a model for studying the laser heating of glass would let to determine the optimal conditions for performing the acquisition (e.g. heating time, cooling time, laser shape, laser power, . . .).

Furthermore, since the material will be heated by the laser, it is necessary to ensure that the operating conditions are such that the material characteristics will not be altered (i.e. burning or melting the material, creating fractures or degrading any of the

surface properties).

By predicting the material behavior it will be ensured that the experiments are carried out safely, and by creating a simulation suite other future possibilities, such as estimating the emissivity from multiple view synthetic images for determining the true temperature of 3D objects, could be explored.

It must be mentioned that the infrared camera only captures the apparent temperature of the object. In order to determine the true surface temperature, some corrections have to be applied and this is the reason why studying techniques for mapping the surface emissivity would be useful. However, for the purposes of this thesis, the camera is not used for determining the temperature, but only for acquiring the object's shape. The only requirement is that the camera is sensitive enough to detect the minimum temperature variation generated by the laser, which will usually be restrained to only a fraction of a degree Kelvin.

Model equations

Many authors have studied the laser heating of glass [14, 27, 18, 23, 15]. Jiao and Wang [14], similarly to Tian and Chu [27], explored the possibility of considering the laser as a volumetric heating source and also as a superficial source. As the experimental results revealed, the latter assumption suffices for our analysis.

The following additional assumptions will be made:

1. Since we are working in a narrow temperature range, around the room temperature, glass is considered isotropic and all the thermodynamic parameters of glass are temperature independent.
2. The temperature is lower than the transition temperature of soda-lime glass (Table 2.1), and the tension stress is lower than the critical value of the fracture (70 MPa). Hence, the phase change and the cutting groove are not considered.
3. Heat transfer is not affected by thermal expansion. Inertia effects are negligible.
4. The CO₂-laser beam is regarded as a surface heating source [27].
5. The superficial heat irradiation is negligible in the area without laser heating.

According to the previous assumptions and with the reference system shown in figure 2.6, the following system of differential equations can be established [12]:

$$\underbrace{\rho c \frac{\partial T}{\partial t}}_{\text{Heat equation}} = k \nabla^2 T \quad (2.4)$$

$$\underbrace{T(0)}_{\text{Initial conditions}} = T_0 \quad (2.5)$$

$$\underbrace{-k \frac{\partial T}{\partial z}}_{\text{Conduction}} + \underbrace{h(T - T_{ext})}_{\text{Convection}} + \underbrace{\sigma \epsilon (T^4 - T_{ext}^4)}_{\text{Radiation}} = \underbrace{\alpha I(x, y, z, t)}_{\text{Irradiation}}, \quad \text{at } z = 0 \quad (2.6)$$

$$\underbrace{-k \frac{\partial T}{\partial n}}_{\text{Conduction}} = \underbrace{h(T_n - T_{ext})}_{\text{Convection}}, \quad \text{outside the laser spot} \quad (2.7)$$

, where k is the thermal conductivity of glass, c and ρ are the heat capacity and the material density, T_0 is the initial temperature of glass, T_{ext} is the environment temperature, T_n denotes the temperature of the area without laser heating, h is the convection heat-transfer coefficient with air, σ is the Stefan-Boltzmann constant, $I(x, y, z, t)$ is the density of the laser power, α is the absorption coefficient and n is the direction cosine of a boundary.

The density I of the laser power can be described by Gaussian distribution and an impulse function, so that for a laser with optical power P_0 :

$$I(x, y, z, t) = \frac{P_0}{\pi r^2} \delta(z) \forall x^2 + y^2 < r^2 \in \Re \quad (2.8)$$

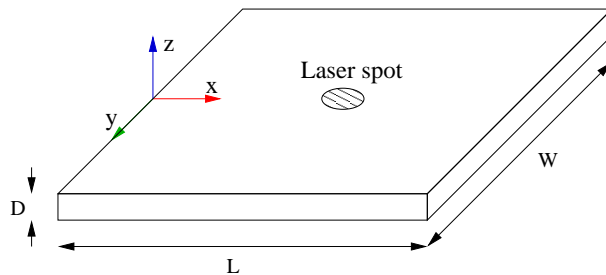


Figure 2.6: Diagram of a piece of glass irradiated by a CO2 laser beam.

In the following section a method for obtaining an approximated solution to the previous equations will be introduced.

2.2.2 Material behavior simulation (FEA Fundamentals)

In order to obtain a value of the temperature at different times t , an approximated technique known as the “finite element method” has proved to be useful for finding approximate solutions of partial differential equations (PDE), as well as of integral equations, such as our heat transfer problem.

In finite element analysis, the model is discretized in such a way that it is possible to approximate the system by solving ordinary differential equations using standard numerical methods such as Euler’s method, Runge-Kutta or others (i.e. successive approximations of the derivatives are performed).

Fortunately, nowadays there is a wide variety of software available in order to perform these approximations at a very high level, using several slope approximation techniques, time sampling approaches and stabilization algorithms. For this work, the open source project “Elmer” [2] from the Finnish IT center for science (CSC) was chosen for simulation, mainly because it is freely available. The technical details of the simulation process will be introduced in chapter 3.

Moreover, by using FEA it is possible to solve very complex geometrical configurations that would be impossible to analyze with non-approximated methods. This could be used for improving the scanning performance (e.g. by studying the laser line projection on a specific structure of interest). Another option is to use a non-uniform discretization of the problem domain, in order to achieve higher resolutions at some interest points, such as the laser spot, but also to work with feasible processing times by reducing the nodal density at less important locations.

Some of the basic steps of this method are the following:

1. Represent the physical system as a nodal network.
2. Use an energy balance to obtain a finite-difference equation for each node.
3. Solve the resulting set of algebraic equations for the unknown nodal temperatures at each time step.

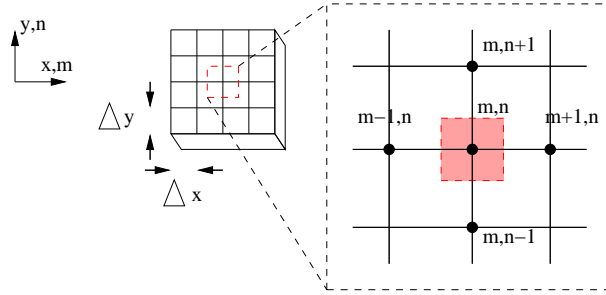


Figure 2.7: Example of a 2D nodal network.

Figure 2.7 shows a 2D nodal network which could represent one section of the glass surface. It identifies discrete points where the temperature should be evaluated. A finite difference approximation is used to represent temperature gradients:

$$\begin{aligned} \left. \frac{\partial T}{\partial x} \right|_{m-1/2,n} &= \frac{T_{m,n} - T_{m-1,n}}{\Delta x} \\ \left. \frac{\partial T}{\partial x} \right|_{m+1/2,n} &= \frac{T_{m+1,n} - T_{m,n}}{\Delta x} \end{aligned}$$

It is evident that the accuracy of the solution depends on the construction of the nodal network. As an arbitrary rule to avoid errors, all heat flows are assumed to be into the nodal region of interest. In this case the energy balance becomes $E_{in} + E_{generated} = 0$.

For instance, case 1 of Figure 2.8 shows the equations that can be derived for an interior point which only exchanges heat with four other nodal points by conduction.

More generally, there are different types of nodal equations. Some basic configurations are shown in the other cases of Figure 2.8. More tools, such as the use of shape factors for accounting radiation exchange, are not developed in here since they were not used in the simulations (only idealized radiation was considered). Nevertheless, the existing FEA software already takes into account this considerations and it is possible to model the interaction between the object and any enclosure that could be used for controlling the environment, with the objective of avoiding the influence of external radiation sources.

After successively approximating the object's temperature at different times, we have a concrete idea of the type of image that the camera will capture. Therefore, to conclude this chapter, the basic theory used for 3D infrared laser scanning will be explored below.

2.3 3D laser scanning

So far, the objective has been to use a laser source for which materials, such as glass, will no longer allow the radiations to pass through or to completely reflect them (i.e. the material will be opaque to some degree). Since with the available CO2 laser source the suitable imaging sensors should also be protected from direct reflections, we are obliged to turn-off the laser and then analyze the heating pattern created by the laser. The use of a model allows us to determine the optimal parameters for capturing and image without altering the object's surface.

It is now necessary to study the tools for triangulating the 3D surface coordinates by studying the deformation of the projected heating pattern.

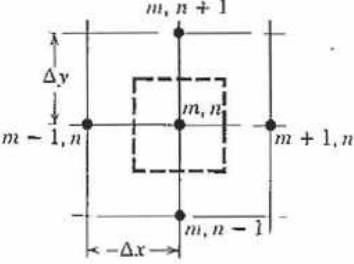
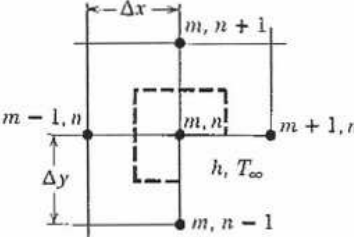
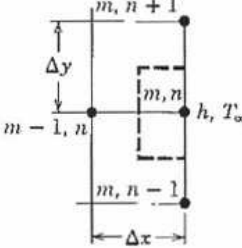
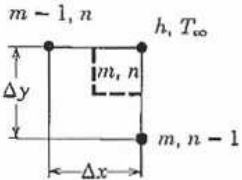
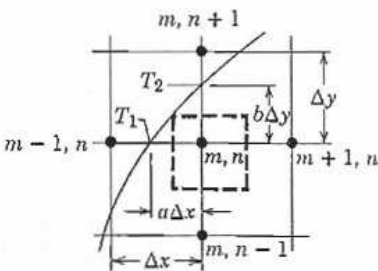
2.3.1 Laser peak detection

As in the case of a standard laser scanner, a laser peak detection method is required for determining the image pixels where the laser pattern is located. As usual, the laser beam is shaped as a plane and a laser line should be extracted from the images. By studying the line deformations it is possible to determine the depth of the surface.

The works of Forest et al. [7] and Fisher et al. [6] present an introduction to laser peak detection in 3D laser scanners, by describing the importance of having a good peak detection algorithm, and also discussing some of the typical noise sources (i.e. electrical noise, quantization noise and speckle). The implemented approach is similar to the one in [7].

The goal is not to design an optimal peak detection method, but to present a general solution for demonstrating that such an infrared laser scanner is feasible.

Since the object to be scanned is initially at temperature T_0 , and after projecting a laser plane the temperature along the intersection with the object's surface will rise, this pattern will be deformed with respect to an additional reference plane that will be used for calibration.

CONFIGURATION	FINITE-DIFFERENCE EQUATION FOR $\Delta x = \Delta y$
	$T_{m,n+1} + T_{m,n-1} + T_{m+1,n} + T_{m-1,n} - 4T_{m,n} = 0 \quad (4.32)$ <p>Case 1. Interior node.</p>
	$2(T_{m-1,n} + T_{m,n+1}) + (T_{m+1,n} + T_{m,n-1}) + 2\frac{h\Delta x}{k}T_{\infty} - 2\left(3 + \frac{h\Delta x}{k}\right)T_{m,n} = 0 \quad (4.44)$ <p>Case 2. Node at an internal corner with convection.</p>
	$(2T_{m-1,n} + T_{m,n+1} + T_{m,n-1}) + \frac{2h\Delta x}{k}T_{\infty} - 2\left(\frac{h\Delta x}{k} + 2\right)T_{m,n} = 0 \quad (4.45)^a$ <p>Case 3. Node at a plane surface with convection.</p>
	$(T_{m,n-1} + T_{m-1,n}) + 2\frac{h\Delta x}{k}T_{\infty} - 2\left(\frac{h\Delta x}{k} + 1\right)T_{m,n} = 0 \quad (4.46)$ <p>Case 4. Node at an external corner with convection.</p>
	$\frac{2}{a+1}T_{m+1,n} + \frac{2}{b+1}T_{m,n-1} + \frac{2}{a(a+1)}T_1 + \frac{2}{b(b+1)}T_2 - \left(\frac{2}{a} + \frac{2}{b}\right)T_{m,n} = 0 \quad (4.47)$ <p>Case 5. Node near a curved surface maintained at a nonuniform temperature.</p>

^aTo obtain the finite-difference equation for an adiabatic surface (or surface of symmetry), simply set h equal to zero.

Figure 2.8: Summary of nodal finite difference equations considering 2D steady state conduction and convection.

In order to segment the interest region (i.e. laser line) it is only necessary to threshold the image at a given temperature value which could be selected by analyzing the image histogram. According to the energy conservation principle, under the absence of any other heat sources, it is guaranteed that the temperature gradient at the laser intersection will be maximum.

Therefore, the laser peak is found by computing the zero-crossing of the segmented temperature gradient along the x direction (i.e. the first derivative along the segmented image rows). As it is shown in figure 2.9, the zero-crossing corresponds to the position of the signal's peak.

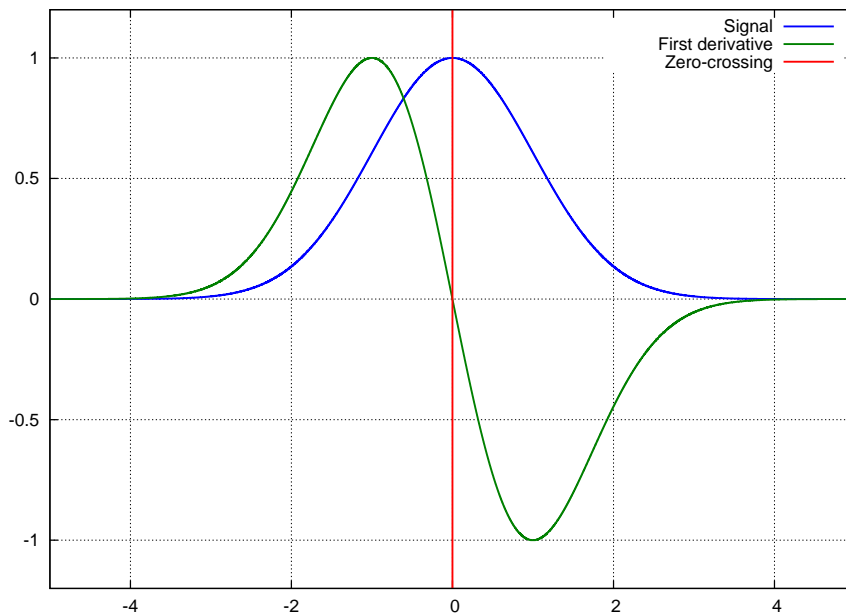


Figure 2.9: Laser peak and first derivative.

The details of thresholding the image and computing the gradient will be presented in chapter 3.

2.3.2 Camera calibration

In order to calibrate the system, composed of the infrared camera and the laser plane, a method which considers both components at the same time would be ideal. Some other calibration techniques perform an initial calibration for obtaining the camera's intrinsic parameters and the location of a reference plane, and then perform a second calibration step for the laser plane (see [16]). This approach may represent an inconvenient. Apart from having to design a custom infrared calibration rig, the imaging parameters have to be setup for the first camera calibration. We cannot assume that the resulting configuration will be optimal during the following step, considering that the detection

of the infrared laser plane, which corresponds to a slight temperature change around the initial temperature, has to be guaranteed.

In spite of the fact that infrared cameras are expensive devices and geometrical distortions are usually small, it would be ideal to use a technique which could account for possible distortions. Although this feature was not taken into account for the prototype, towards the end of this work a method for handling distortions will be discussed.

Below, a calibration technique will be reviewed. This approach seems to satisfy our requirements by using the cross-ratio and the complete quadrangle definitions.

The complete quadrangle technique

The implemented technique is based on the work of Joseph Forest from the Universitat de Girona [13]. It is based on elementary concepts from projective geometry [24, 21] that will be discussed in this section.

Let's first introduce the cross ratio of a pencil of four lines, defined by the four points of intersection of a fourth line, not penetrating the pencil. The intersection points A, B, C and D are shown in Figure 2.10. Equations 2.9 and 2.10 define the cross ratio, where λ_1 , λ_2 and λ_3 refer to the distances \overline{AB} , \overline{AC} and \overline{AD} , respectively. It can be demonstrated that under projective transformations, the cross-ratio is invariant, and equations 2.11 and 2.12 are useful for determining any fourth projected point from the knowledge of only three points.

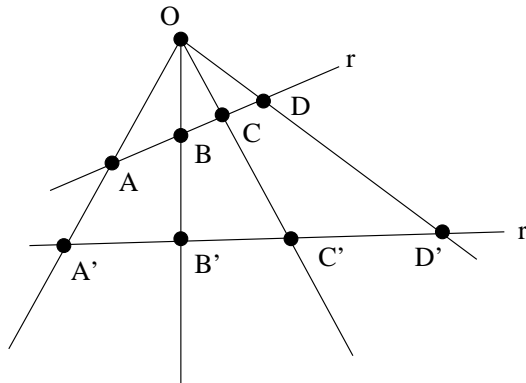


Figure 2.10: Cross-ratio of a pencil of lines.

$$Cr\{A, B; C, D\} = \frac{\overline{ACBD}}{\overline{ADBC}} \quad (2.9)$$

$$k = \frac{\lambda_2 \cdot (\lambda_3 - \lambda_1)}{\lambda_3 \cdot (\lambda_2 - \lambda_1)} \quad (2.10)$$

$$\lambda'_2 = \frac{k \cdot \lambda'_3 \cdot \lambda'_1}{(k - 1) \cdot \lambda'_3 + \lambda'_1} \quad (2.11)$$

$$r = \lambda_i \cdot \frac{D - A}{\|D - A\|} + A \quad (2.12)$$

The complete quadrangle on the other hand, is any set of four non-aligned points, as shown in figure 2.11. It defines 7 points in total, A to G, and the pencil of four lines based at intersection of opposite sides is harmonic. For instance, $Cr\{FA, FB; FE; FG\} = -1$.

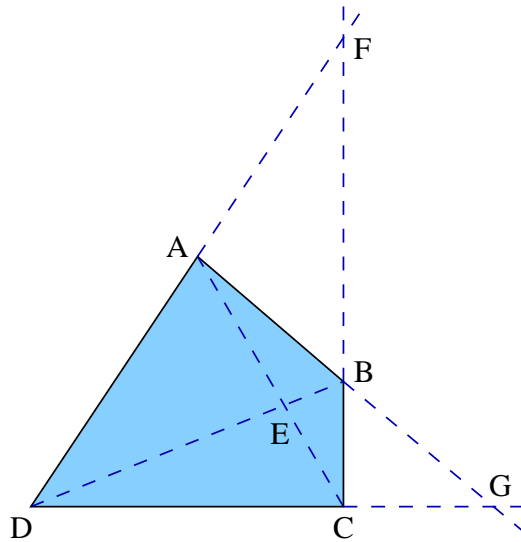


Figure 2.11: The complete quadrangle.

In order to calibrate the system we would like to find a transformation ${}^W T_L$ between the 3D surface points and the extracted image points. This can be linearly approximated by:

$$\begin{bmatrix} sX \\ sY \\ sZ \\ s \end{bmatrix} = {}^W T_L (4 \times 3) \cdot \begin{bmatrix} u \\ v \\ 1 \end{bmatrix} = \begin{bmatrix} t_{11} & t_{12} & t_{13} \\ t_{21} & t_{22} & t_{23} \\ t_{31} & t_{32} & t_{33} \\ t_{41} & t_{42} & t_{43} \end{bmatrix} \cdot \begin{bmatrix} u \\ v \\ 1 \end{bmatrix} \quad (2.13)$$

Arranging and grouping the terms, an homogeneous system of 3 equations with 12 unknowns is obtained, and it can be solved by minimizing equation 2.14, where the terms X_i , Y_i and Z_i refer to the 3D coordinates, and u , v to the 2D image coordinates of the correspondences. A good estimation using the Total Least Square technique, available in any numerical computing library, is calculated from the eigenvector corresponding to the smallest eigenvalue of matrix $A^T \cdot A$.

$$\begin{matrix}
 \begin{bmatrix}
 \vdots & \vdots & \vdots & \vdots & \vdots & \vdots & \vdots & \vdots & \vdots & \vdots & \vdots \\
 u_i & v_i & 1 & 0 & 0 & 0 & 0 & 0 & -u_i \cdot X_i & -v_i \cdot X_i & -X_i \\
 0 & 0 & 0 & u_i & v_i & 1 & 0 & 0 & -u_i \cdot Y_i & -v_i \cdot Y_i & -Y_i \\
 0 & 0 & 0 & 0 & 0 & 0 & u_i & v_i & -u_i \cdot Z_i & -v_i \cdot Z_i & -Z_i \\
 \vdots & \vdots & \vdots & \vdots & \vdots & \vdots & \vdots & \vdots & \vdots & \vdots & \vdots
 \end{bmatrix} & \cdot & \begin{bmatrix}
 t_{11} \\
 t_{12} \\
 t_{13} \\
 t_{21} \\
 t_{22} \\
 t_{23} \\
 t_{31} \\
 t_{32} \\
 t_{33} \\
 t_{41} \\
 t_{42} \\
 t_{43}
 \end{bmatrix} & = & \begin{bmatrix}
 \vdots \\
 0 \\
 0 \\
 0 \\
 \vdots
 \end{bmatrix} \\
 A & & \theta & = 0 & (2.14)
 \end{matrix}$$

In order to find the required 2D-3D correspondences for solving equation 2.14, the complete quadrangle is used. Equations 2.11 and 2.12 are applied systematically, as it will be detailed in Chapter 3. Figure 2.12 illustrates that if A,B are known 3D points, and A', B' and Pa' can be found analyzing the acquired image, Pa can be determined by the cross-ratio principle. The same principle can be applied for point Pb. If the quadrangle is moved along the z-axis (i.e. at different depths), a set of 2D-3D correspondences can be found for each depth.

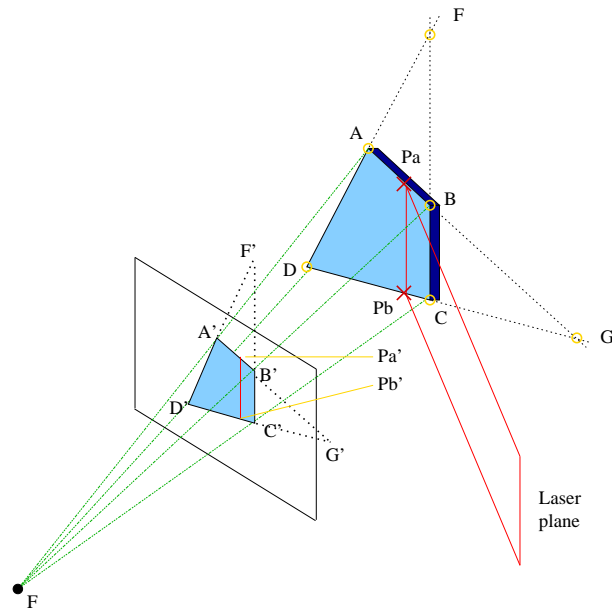


Figure 2.12: Determination of 2D-3D correspondences using the complete quadrangle.

2.3.3 Triangulation using the complete quadrangle technique

Triangulation is a straight forward step, since from equation 2.13 is evident that once ${}^W T_L$ is known, 2D points in the image frame can be directly transformed to 3D points in the world reference frame by a simple matrix dot product operation.

As a previous step, the 2D image points are uniquely determined by using the previously proposed laser peak detection method.

Chapter 3

Solution

This chapter deals with the solution of the two main project tasks, which are:

1. Developing a method for simulating the laser heating process, in order to determine the optimal image acquisition parameters.
2. Describing the prototype scanning system hardware, the software library specifications and the implemented 3D surface acquisition algorithms.

3.1 Finite Elements Analysis

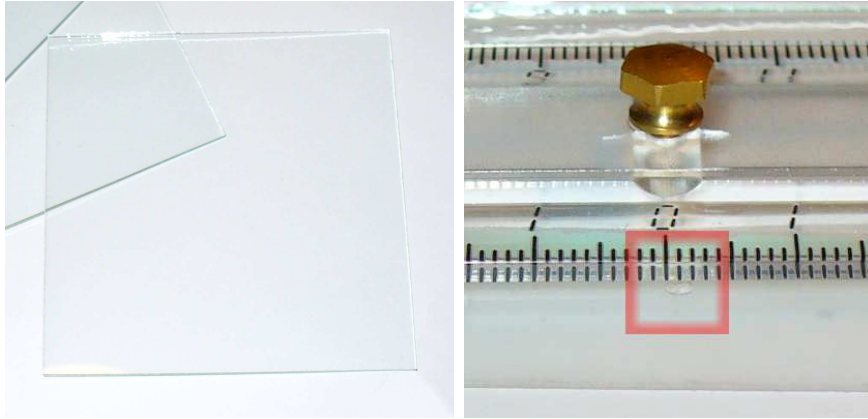
In order to solve the heating model presented for the first time in section 2.2.2, the open-source finite elements analysis software Elmer [2] was employed.

The first step for solving our heating problem using FEA, is to define the geometry of the sample. The piece of glass used for the experiments, shown in figure 3.1, measures $10cm \times 10cm \times 2mm$. Additionally, the laser spot diameter, according to the specifications given by the manufacturer, is $\phi = 2.4mm$.

By using the Salome platform [25], which is a free software project compatible with Elmer, and the previously defined dimensions, the geometry was defined as the union of a rectangular prism, and a cylinder of diameter ϕ . Figure 3.2 illustrates the resulting configuration. At this point different groups of faces were defined, in order to later apply the boundary conditions. Four groups were created and names as: boundary1 (laser spot), boundary (remaining top face), boundary3 (the sides) and boundary4 (the bottom face). This names will be used in the simulation description files for Elmer.

After defining the geometry, the next step is to generate a 3D mesh of nodes by choosing some of the available mesh generation algorithms. A non-uniform mesh was selected in order to achieve a higher temperature resolution at the laser spot, while still keeping an acceptable processing time since the resolution at other less important areas was reduced. Figure 3.3 presents the generated mesh.

The resulting mesh, or nodal network, has to be saved and converted to a file format which is compatible with Elmer. This is performed by first saving the mesh using a common 3D graphics CAD-CAM format known as UNV, and then converting it to



(a) Photography of the sample. (b) A piece of tape burned by the laser spot.

Figure 3.1: Sample of glass

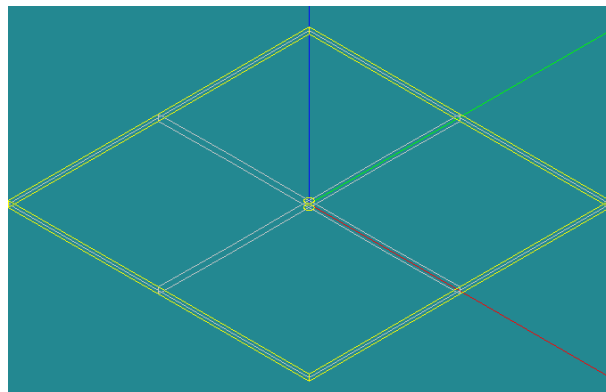
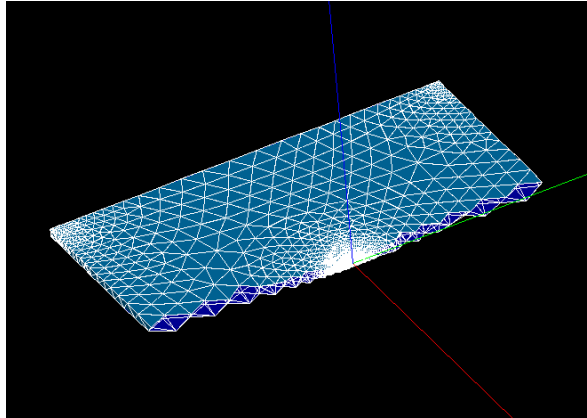
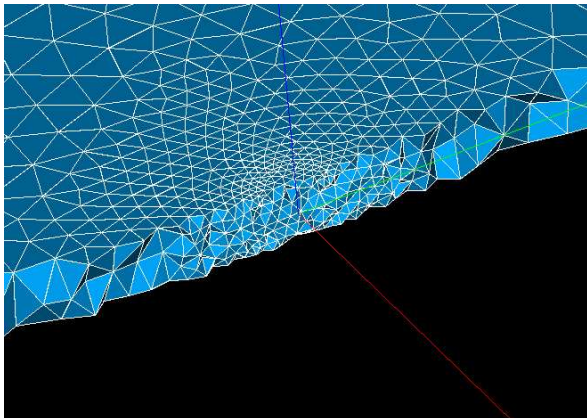


Figure 3.2: Geometry definition



(a) 3D mesh of nodes.



(b) Amplification of the laser spot.

Figure 3.3: 3D mesh generation for FEA

a compatible format such as the GMSH extension. For this purpose a script named “unv2gmsh.py” was developed. Please refer to appendix A for accessing the simulation files.

After loading the generated mesh in ElmerFront, a GUI interface is used for setting up the simulation parameters (i.e. ElmerFront), and then a description file for the simulation is generated. This file, with the “.sif” extension, is the one required by the command line solver (ElmerSolver) and it can be found in appendix A.

Basically, the heat equation is setup according to section 2.2.2. Some key features of the setup are:

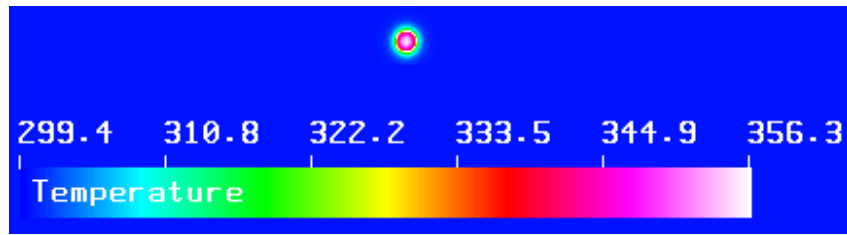
- The initial temperature, measured during the experiments, is set to $300K$.
- The glass material parameters are obtained from Table 2.1.
- The heat flux for the laser spot boundary condition (boundary1) is set according to equation 2.8 so that it corresponds to a laser optical power of $400mW$ (according to the manufacturer’s datasheet).
- A convection heat transfer coefficient of $10W/(m^2K)$ is assumed.
- The external temperature is set to $300K$.
- Only idealized radiation is considered, using an emissivity value $\epsilon = 0.92$.
- A time-step of $20ms$, which corresponds to the minimum acquisition period of the infrared camera, and a total simulation time of $7s$ are set.

For the purposes of this simulation, the laser source was applied for a duration of $1s$, from $t = 0.24s$ until $t = 1.24s$. Figure 4.2 shows some results at $t = 1.24s$, which correspond to the maximum simulated heating. The reason why this parameters were chosen is that, in the next chapter of experimental results, a real video sequence with the same characteristics was recorded. This will allow us to make a comparison in order to validate the heating model.

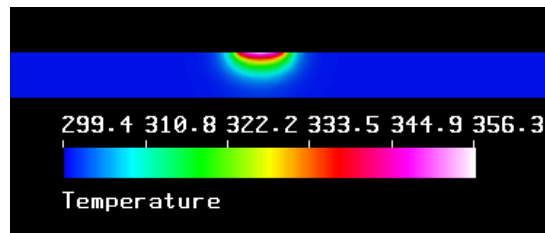
It should be remarked that using this tools is not only possible to predict the temperature at the surface, but we could also study the volumetric heat transfer process, as in Figure 4.2.b.

It can be concluded that, for the specified parameters, the experiments can be performed safely without altering the properties of the sample under study. A maximum temperature difference of $50K$ should be expected, and the temperature will drop very quickly after turning off the laser. This expected behavior will affect the experimental results, since a device which performs the function of a shutter should be ideally synchronized with the laser, for instantly capturing the maximum temperature gradient. This was not the case of the experimental setup, for which the camera’s protection was removed by hand, and the same situation applies to the laser source activation.

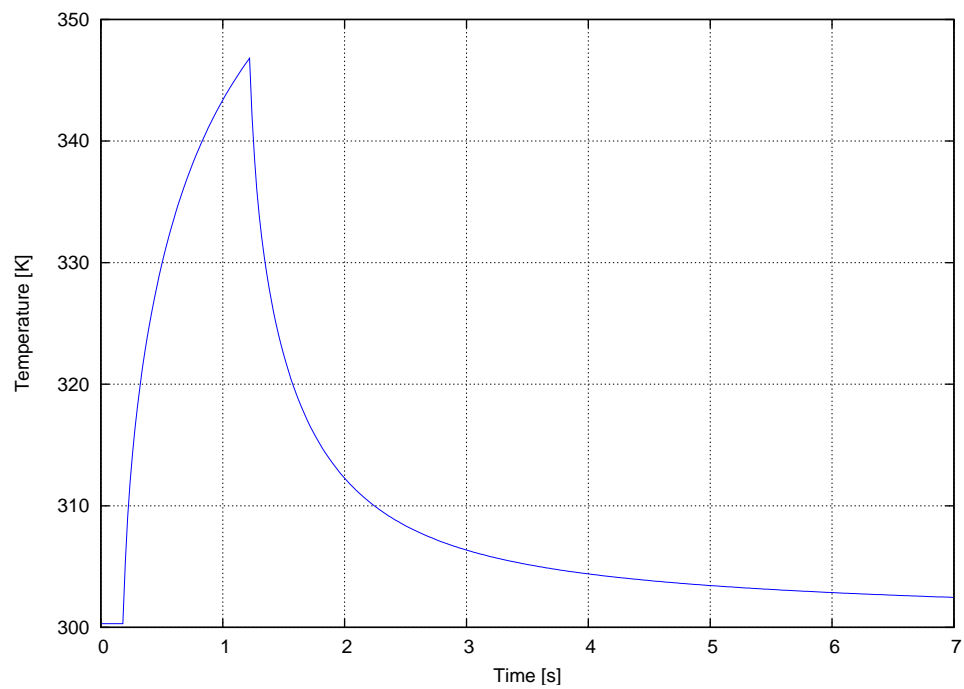
After having considered the essentials for performing a simulation, a detailed description of the infrared laser scanning prototype will be finally given.



(a) Front view of the simulation results at $t = 1.24s$.



(b) Transversal cut to visualize the volumetric heat transfer.



(c) Simulated average temperature evolution at the laser spot.

Figure 3.4: 3D mesh generation for FEA

3.2 3D infrared laser scanning

Figure 3.5 shows a diagram of the prototype infrared laser scanning system that was available. Until now, two problems were identified (i.e. the absence of a precise time control for switching or deviating the laser, and the manual synchronization between the laser and the camera). As an advance of the next chapter, it should also be mentioned that the available cylindrical lens for generating the plane is such that for correctly focusing a line, the distance from the object D should be kept in the order of $2.5m$, which implies a big working space for performing the experiments. Finally, some sections of the imaging sensor were already damaged and, thus, the image processing becomes more tedious.

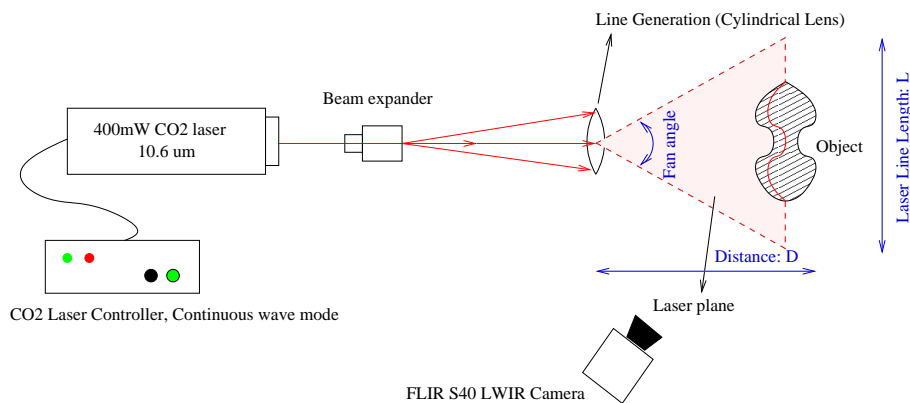


Figure 3.5: Diagram of the prototype laser scanning system.

In order to perform the 3D scanning process, an object-oriented library was developed. All the routines were written using the Python programming language [8], instead of Matlab, since object-oriented programming is a more natural way to work (e.g. from the definition of a point, a line is defined, then a plane, then the geometry of the complete quadrangle, . . .).

Other advantages over Matlab are:

1. The software is easier to reuse and port to any other object-oriented languages such as C++.
2. Matlab is like C, a procedural programming language which is function oriented.
3. Python is faster and it can be more precise than Matlab.
4. Python is a very high level language and this allows to speed-up the development process.
5. It supports complex server applications.

3.2.1 Library specifications and requirements

The requirements for running the library are:

- A previous installation of Python [8], and the PyQt, PIL (Python Imaging Library) and Scipy/Numpy packages [22]. The latter packages, provide the basic tools for creating GUIs or performing mathematical operations such as least squares regression, singular value decomposition, matrix manipulations, etc.
- The library was developed and documented using the Eclipse Integrated Development Environment [9] with the PyDev module.
- Windows or Linux operating systems.

Six main modules compose the library:

1. CQCornersWidget.py, which provides a GUI interface for performing the calibration step. The calibration images, acquired with the infrared camera, have to be copied into the images folder. The graphical interface allows the user to select which images will be used for calibration, to define the specific depth for each image, and to make the initial selection of points that will be used for computing the set of 2D-3D correspondences.
2. Geometry.py, that is used by the GUI interface. It defines objects such as points, lines, image planes, the complete quadrangle, various 2D filters and image windows. The complete quadrangle object has all the methods for adding or removing points, for robustly fitting the laser line or even for extracting corners with subpixel accuracy.
3. Calibrate.py, for computing the ${}^W T_L$ transformation used for triangulation using the computed 2D-3D correspondences, obtained after running the user interface.
4. Reconstruct.py, which performs the triangulation step to generate a points cloud from a sequence of images.
5. Ransac.py, an implementation of the ransac algorithm that was used in the complete quadrangle object for robust fitting of lines.
6. And Utils.py, which contains routines for converting images into arrays, and viceversa, together with the 2D image gradient computation used for laser peak detection.

3.2.2 The complete quadrangle technique

Calibration

In order to perform the calibration step, a complete quadrangle made of glass was manufactured. Several infrared images of this quadrangle were taken at different known depths, as illustrated in Figure 3.6.

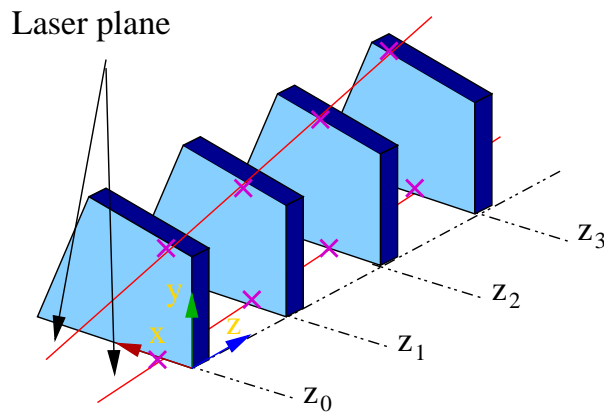


Figure 3.6: Positioning of the complete quadrangle at different known depths

Nevertheless, figure 3.7.a) shows that when projecting the laser line the visibility of the quadrangle corners was far from ideal. By applying some active lightning in order to enhance the corners, figures 3.7.b)-d) were obtained. Any diffuse heating source could be used for this purposes and, if the radiations are well spread, it should be possible to enhance the four corners at the same time in a single-shot. The resulting images are superimposed and the final image in which all the interest points are visible is shown in figure 3.7.e).

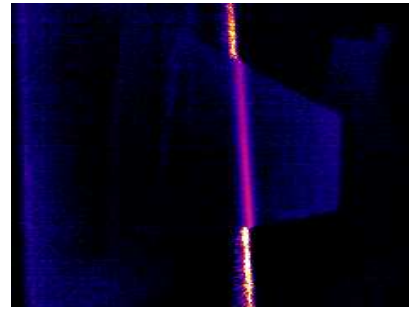
Subsequently, by using the CQCornersWidget GUI, the user is able to set the depth of each image, to define the real glass complete quadrangle dimensions, to initialize the interest points and to save the sets of computed 2D-3D correspondences. The GUI is shown in figure 3.8.

The algorithm for sub-pixel corner detection is based on the cornerness measures defined originally in the Harris corner detector [1].

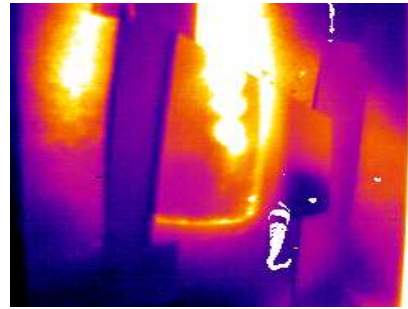
In order to estimate the 2D-3D correspondences, point Pa is the first to be estimated in 3D, since we know the value of the cross-ratio from the 2D image, and also the value of three other 3D points (i.e. A, B and G). Equations 2.11 and 2.12 are directly applied in this case. The same situation applies for Pb and the 3D points C,D and G.

Subsequently, additional correspondences are found by considering the points defined in figure 3.9. By selecting random points P'_L in the segment $A'D'$, it is possible to find the corresponding 3D points P_L by computing the cross ratio value in the image plane (using points F' , A' , D' and P'_L), together with the knowledge of points F , A and D . Then, it is only necessary to find the intersections P'_r and P'_s in the image plane, for posteriorly using once more the cross-ratio relations to compute the most accurate correspondences for P_r and P_s .

After storing the desired 2D-3D correspondences, the user only has to run the script Calibrate.py, which will approximate the transformation ${}^W T_L$ by using the Total Least Squares technique described in chapter 2.



(a) Laser projection over the complete quadrangle



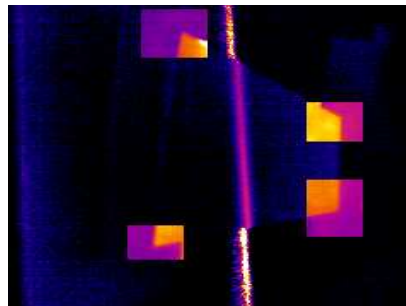
(b) Enhancement of corner A applying external illumination



(c) Enhancement of corners B and C using external illumination

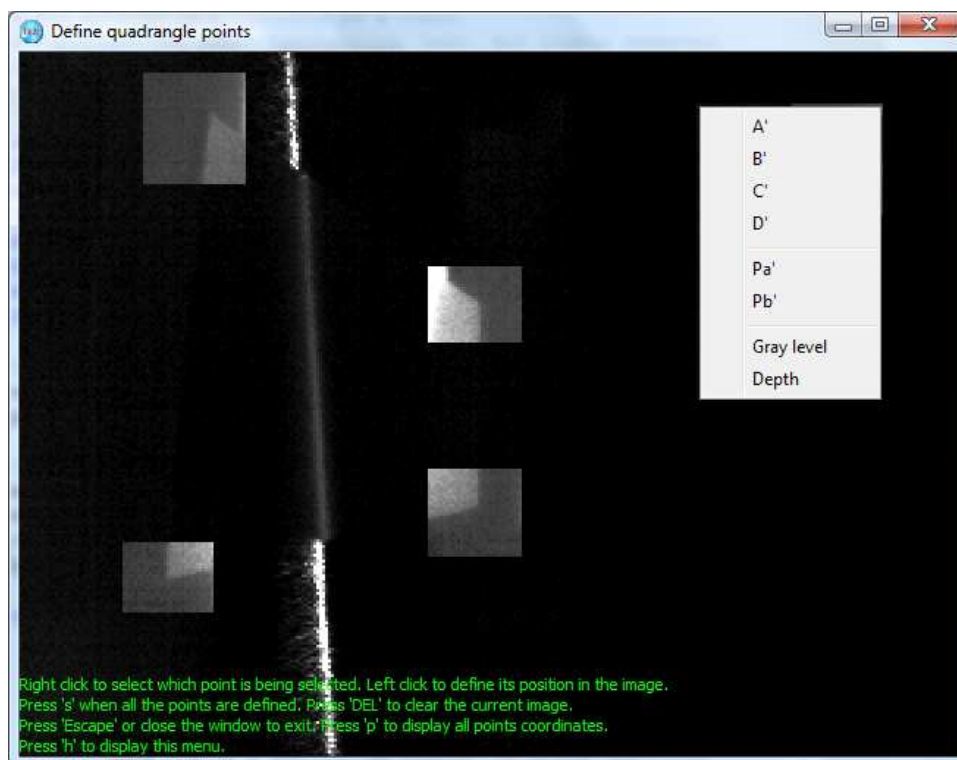


(d) Enhancement of corner D applying external illumination

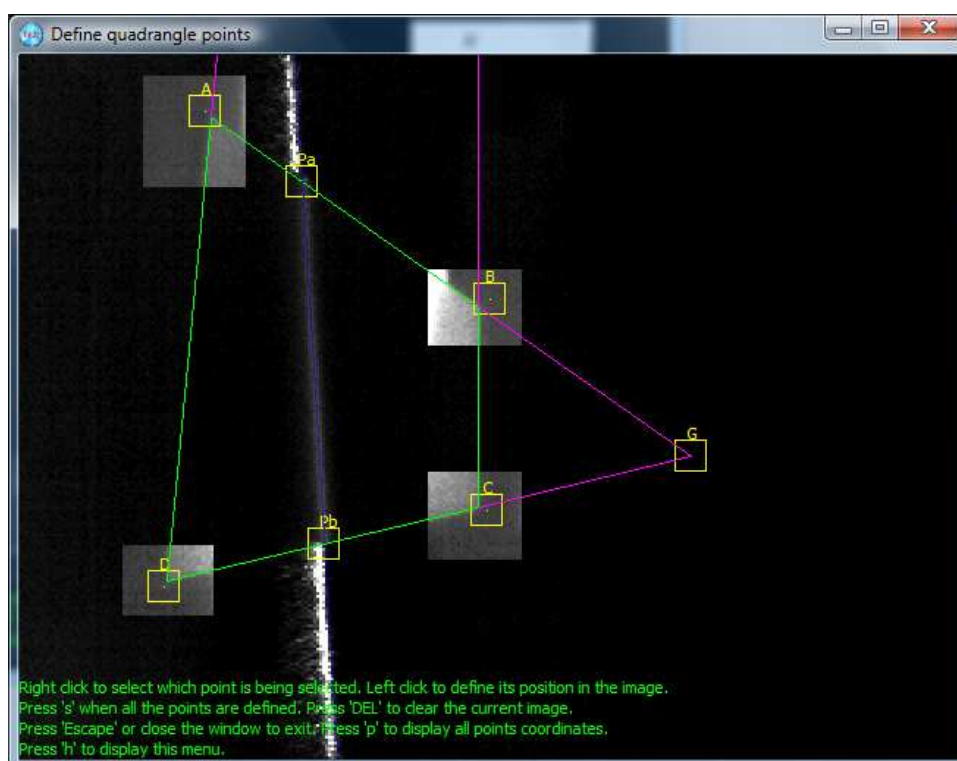


(e) Resulting composed image

Figure 3.7: Enhancement of the complete quadrangle calibration images.



(a) Interface presentation before any user interaction



(b) Example of an analyzed image

Figure 3.8: CQCornersWidget calibration interface.

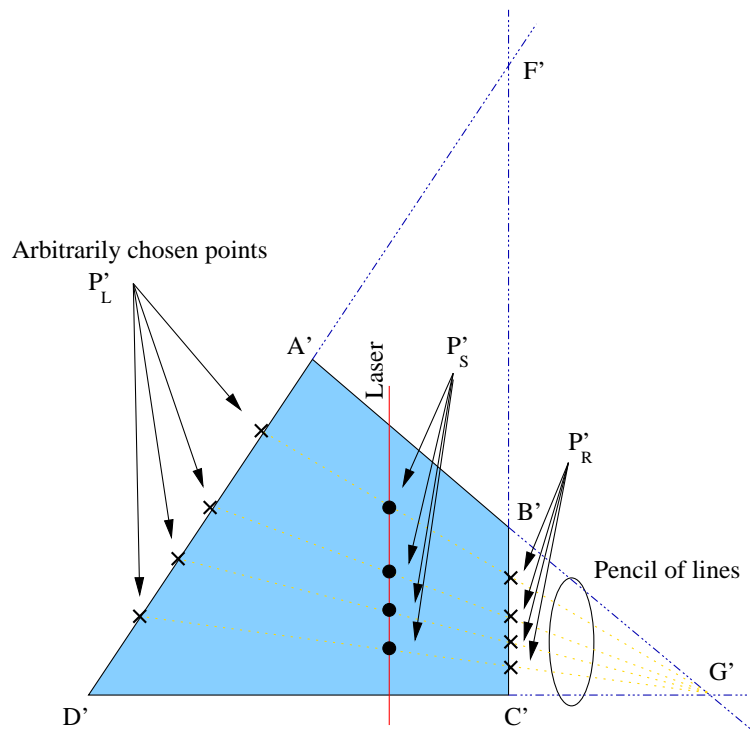


Figure 3.9: Computation of additional correspondence points.

Model fitting

In order to fit the laser line in the complete quadrangle images, a custom implementation of the Ransac algorithm was programmed. This is because some outliers might be present, specially close to the intersection points P'_a or P'_b .

Originally, a simple linear least squares fitting was performed, but figure 3.10 evidences why this method did not suffice. Each of the data points from the figure correspond to the laser peak approximation, obtained by computing the zero-crossing point of the horizontal image gradient. The outliers were obtained mainly because the detected laser-line corresponds to the projection on the metal plate used to hold the complete quadrangle, which is located just behind it.

The pseudo-code of the Ransac algorithm is summarized below.

Ransac algorithm pseudo-code

Given:

`data` - a set of observed data points (first column is independent variable)

`model` - a model that can be fitted to data points

`n` - the minimum number of data values required to fit the model

`k` - the maximum number of iterations allowed in the algorithm

`t` - a threshold value for determining when a data point fits a model

`d` - the number of close data values required to assert that a model fits well to data

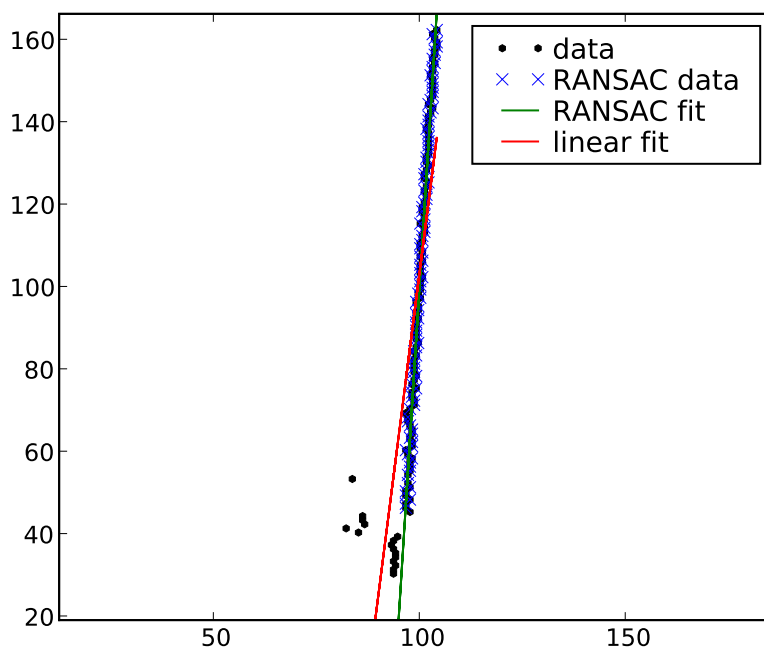


Figure 3.10: Ransac fitting of the laser line during the system calibration.

```

Return:
    bestfit - model parameters which best fit the data (or nil if no good model is found)

iterations = 0
bestfit = null
besterr = maximum possible value (Inf)
while iterations < k {
    maybeinliers = n randomly selected values from data
    maybeamodel = model parameters fitted to maybeinliers
    alsoinliers = empty set
    for every point in data not in maybeinliers {
        if point fits maybeamodel with an error smaller than t
            add point to alsoinliers
    }
    if the number of elements in alsoinliers is > d {
        !this implies that we may have found a good model
        !now test how good it is
        bettermodel = model parameters fitted to all points in maybeinliers and alsoinliers
        thiserr = a measure of how well model fits these points
        if thiserr < besterr {
            bestfit = bettermodel
            besterr = thiserr
        }
    }
    increment iterations
}
return bestfit

```

Reconstruction

In order to perform a reconstruction from a sequence of images, first the deformed laser pattern has to be extracted. Figure 3.11 describes the implemented process in which the image histogram is analyzed for determining an upper value limit for segmenting the maximum temperature change. After segmentation, the horizontal gradient of the image is computed by taking the successive horizontal pixel differences, and then an approximation of the zero crossing is performed in order to find the 2D image coordinates of the laser peak.

Since the transformation ${}^W T_L$ is already known after calibration, the simple dot product will lead to the corresponding 3D points, according to equation 2.13.

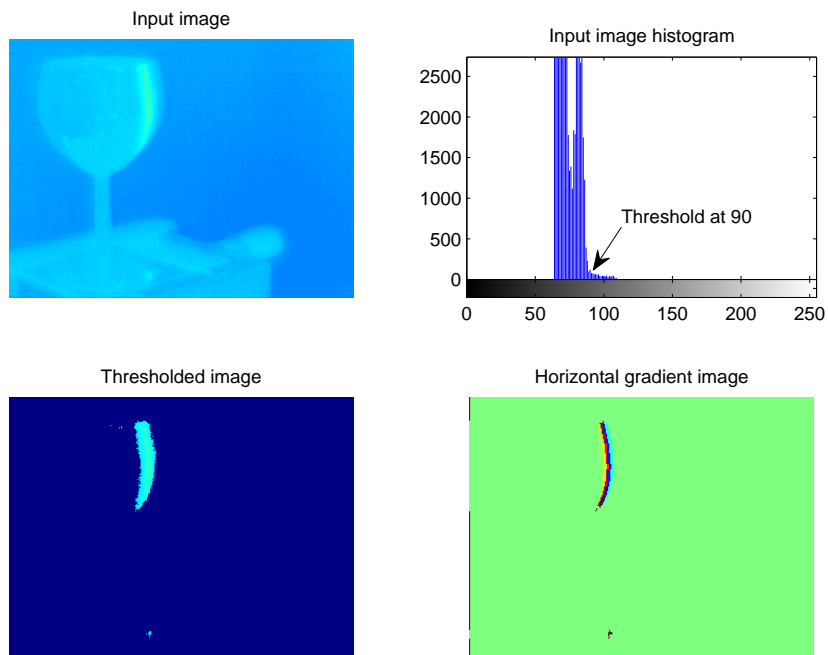


Figure 3.11: Laser peak estimation for triangulation of 3D points.

Chapter 4

Experimental Results and Analysis

4.1 Simulations

4.1.1 Experimental setup

The experimental setup used for verifying the accuracy of the proposed heating model is shown in Figure 4.1. The sample of glass is perpendicularly exposed to laser irradiation and the resulting heat transfer is recorded by the camera.

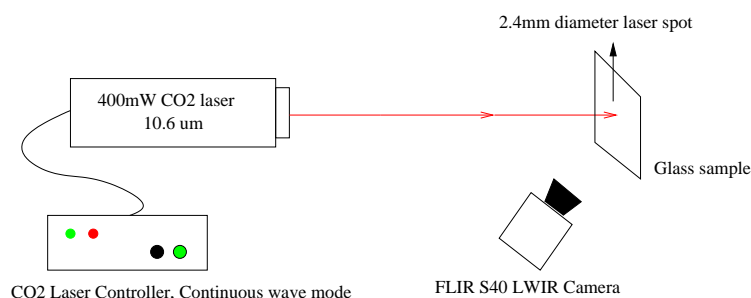


Figure 4.1: Experimental setup for validating the superficial laser heating model.

4.1.2 Validation of the superficial heating model

After acquiring a real video sequence using the same parameters that were established for simulations in the previous chapter, the average temperatures of the laser spot were plotted and compared in figure 4.2. The similarity between the real and the synthetic images is remarkable. Additionally, the general shape of the temperature curves show that the simulated model is very close to the real system behavior.

The main reason why the curves are not identical is that standard thermal values, arbitrarily taken from the literature, were used for the simulation. Instead, it would be ideal to accurately know all the properties of the sample. Moreover, despite an optical power of $400mW$ was assumed, the equipment for determining the real value

was not available. Because the CO₂ laser was new, it is very likely that it exceeds the manufacturer's specifications during the first essays.

If we consider that the temperature changes that will be generated by a laser line will only involve a few degrees kelvin, the obtained margin of error for a very abrupt temperature change of about $50K$ is acceptable.

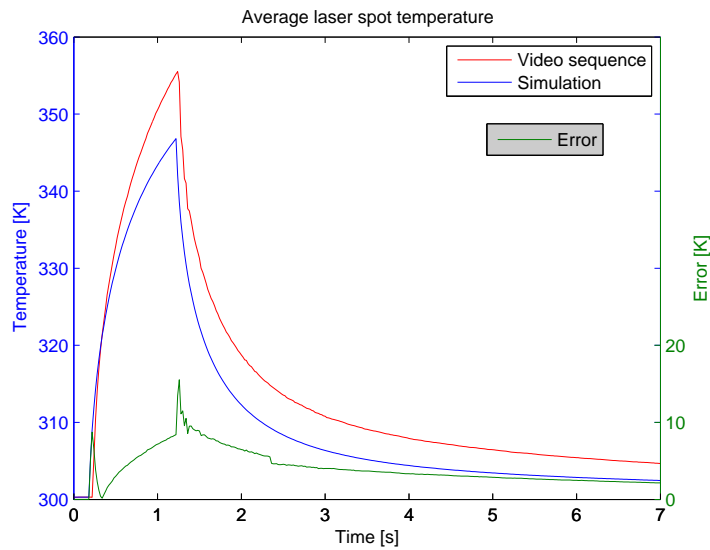
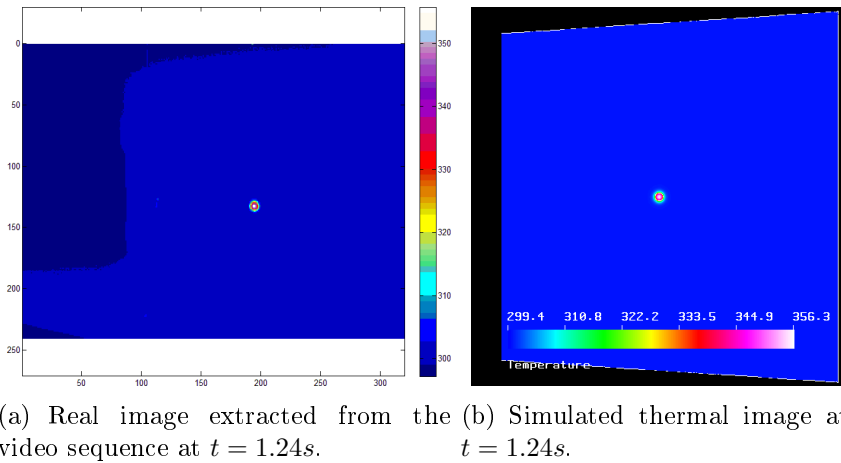


Figure 4.2: Validation results for the superficial laser heating model.

4.2 3D reconstruction

4.2.1 Experimental setup

Figure 4.3 shows the experimental setup, used for laser scanning. From the photography, it is evident that the working space necessary for focusing the laser line was too large ($D \approx 2.5m$) and this should be corrected in the future.

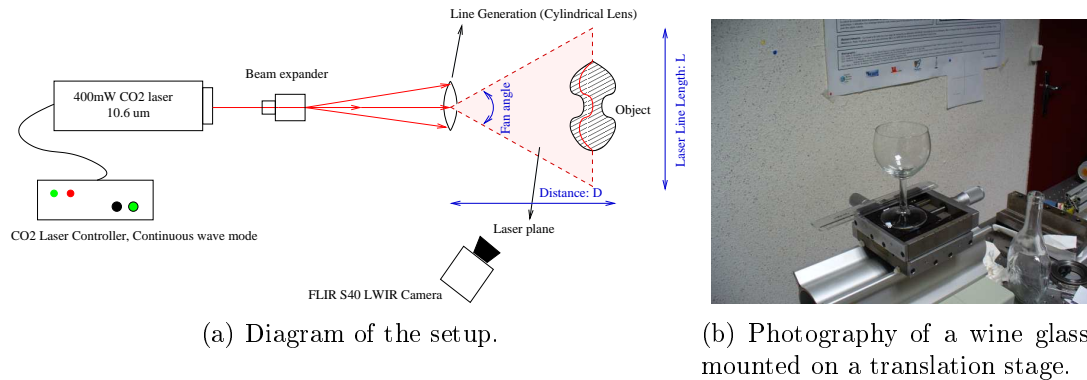


Figure 4.3: Experimental setup for 3D surface surface acquisition.

Figure 4.4 shows the complete quadrangle made in glass.



Figure 4.4: Complete quadrangle in glass.

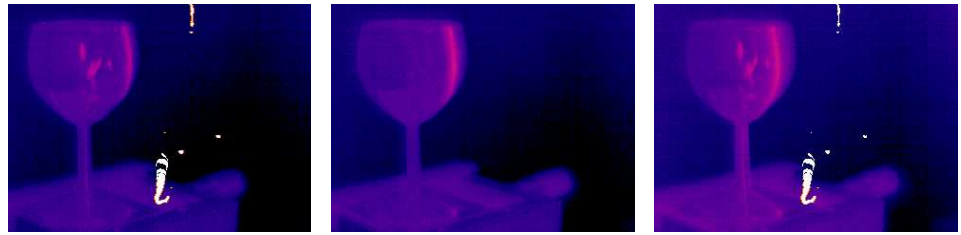
4.2.2 Triangulation results

In order to perform a complete 3D reconstruction, very dense clouds of points have to be acquired for generating a mesh by applying, for instance, a delaunay triangulation filter. However, the prototype system already required a very big working space and it was not possible to accurately translate the sample since a positioning stage with scales was not available. As a result, it was only possible to acquire some non-uniformly spaced point clouds, by using steps of $5mm$ along the x direction.

An example image sequence which corresponds to a wine glass is presented in figure 4.5. It is evident that the burned pixels of the camera will represent an issue for further processing, and that there are other external heat sources interfering with the measurement of the laser pattern. These sources correspond to the people inside the laboratory, and they could easily be removed by designing an enclosure, such as a dome. The only image that was digitally retouched for further processing is the one acquired at $x = 5mm$.

After processing the image sequence using the `Reconstruct.py` script, figure 4.6 shows the final triangulation results. The shape of a section of the wine glass can be easily identified.

In order to have an idea of the metric accuracy of the obtained points cloud, some distances were measured directly in the object (figure 4.7.a), and these values were compared with measurements made using the triangulated points. Table 4.1 summarizes the results. In general, from these few measures it is not possible to determine the accuracy of the reconstruction, and this should be assessed in the near future.



(a) Wine glass at $x = 0mm$ (b) Wine glass at $x = 5mm$ (c) Wine glass at $x = 10mm$



(d) Wine glass at $x = 15mm$ (e) Wine glass at $x = 20mm$ (f) Wine glass at $x = 25mm$

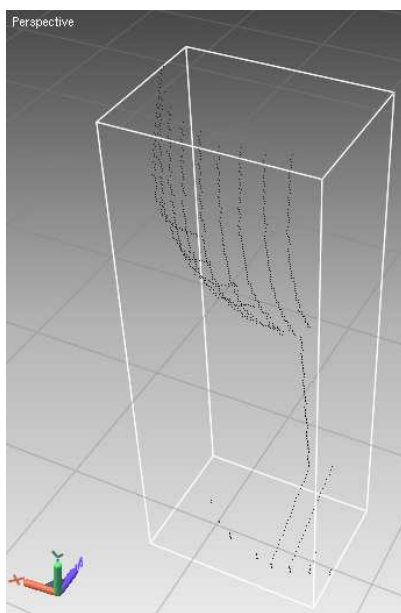


(g) Wine glass at $x = 30mm$ (h) Wine glass at $x = 35mm$ (i) Wine glass at $x = 40mm$

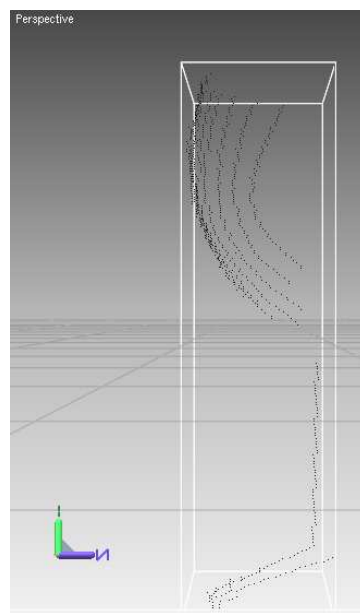
Figure 4.5: Example of an input image sequence.



(a) Wine glass photography



(b) Perspective view of the acquired cloud of points

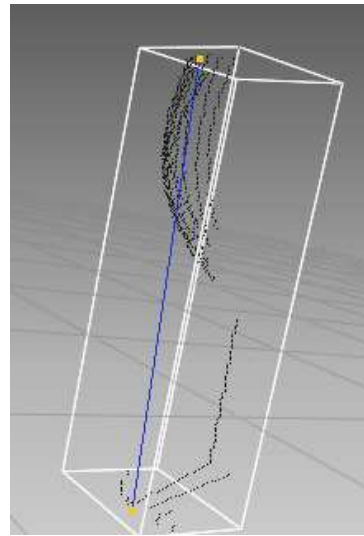


(c) Left view of the acquired cloud of points

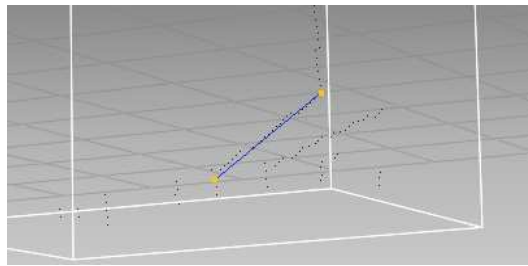
Figure 4.6: Triangulation results for a wine glass.



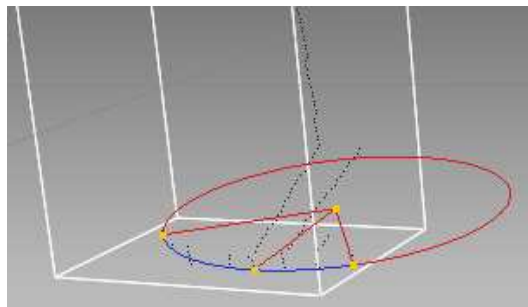
(a) Distance from the base to the border of the glass



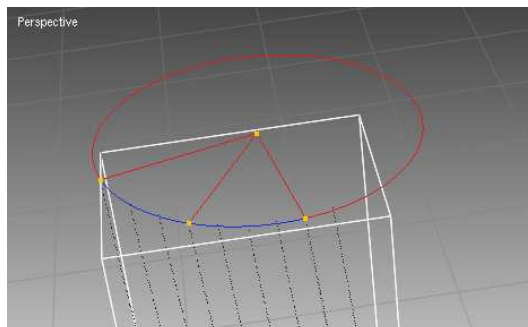
(b) Distance measured using a caliper



(c) Distance along the base



(d) Base diameter



(e) Top cavity diameter

Figure 4.7: Accuracy of the point clouds.

Distance from figure 4.7	Direct measurement	Points cloud measurement
b), Along the vertical axis of the cup	130.1mm	129.0mm
c), Along the base of the cup	29.5mm	29.1mm
d), Diameter of the base	60.1mm	58.8mm
e), Top cavity diameter	62.0mm	62.4mm

Table 4.1: Comparison of values measured directly using a caliper and using the triangulated points

Chapter 5

Conclusions and future work

The main contribution of this thesis consists of having demonstrated that it is possible to acquire the shape of non-opaque objects by studying the behavior of materials outside the visible light spectrum. If all the technical limitations of the experimental setup are considered, it was possible to obtain accurate point clouds of transparent glass objects by using a prototype system that only required a single long-wave infrared camera and a CO₂ infrared laser.

Well known triangulation techniques were successfully applied for analyzing the heating pattern deformation in order to determine the 3D coordinates of the object's surface, providing a novel and simple method which could match the performance of other approaches such as light polarization, conoscopic holography, dynamic lightning, reflection modeling and other model minimization methods.

The superficial laser heating model of glass was also validated by comparing the simulation results with those of a real sequence. This type of modeling was particularly useful for performing the experiments safely and for optimizing the acquisition procedure.

And finally, future efforts should focus on improving the prototype system by considering the following possibilities:

- Making a programmable control for the laser source, in order to restrict the applied irradiation by blocking or deviating the laser beam.
- Designing a programmable shutter system for the infrared camera, which could be synchronized with the laser operation in order to capture the maximum temperature gradient without damaging the imaging sensor.
- Acquiring new optics which could allow the system to be more compact and to improve the focusing of the laser line.
- Creating a custom base in order to fix the components as much as possible.
- Finding a diffuse heat source that can be used for acquiring the complete quadrangle corners in a single step.

-
- Acquiring a programmable positioning stage in order to accurately scan the sample and to keep track of the complete quadrangle during the calibration stage.
 - Studying the feasibility of working at other infrared spectrum wavelengths and also the possible modification of other types of techniques (e.g. time-of-flight sensors, structured light, etc.).
 - Determining the experimental accuracy of the system.

Appendix A

Finite Elements Analysis using ELMER

All the files used for simulation can be found at: <http://alonso.ss.googlepages.com/msc.vibotmasterthesis>.

The contents of the *.sif file, which is used by the Elmer solver in order to describe the system, is appended below.

Description file for the Elmer software

```
!ElmerSolver input file from ElmerFront
!Saved          = Mon 09 Jun 2008 02:19:59 AM CDT User=caelinux Host=
!Case           = laserHeat laserHeat
!Model dir      = /home/caelinux/Documents/Simulations/glass
!Include path   =
!Results dir    = /home/caelinux/Documents/Simulations/glass
!Bodies 1
!Equations 1
!Solvers 1
!Materials 1
!Body Forces 0
!Initial Conditions 1
!Boundary Conditions 4
!Boundaries 4
!echo on

Header
  CHECK KEYWORDS Warn
  Mesh DB "MESHDIR" "glass"
  Include Path ""
  Results Directory ""
End
```

```
Simulation
  Min Output Level = Integer 0
  Max Output Level = Integer 31
  Output Caller = Logical True

  Coordinate System = String "Cartesian 3D"
  Coordinate Mapping(3) = Integer 1 2 3

  Timestepping Method = String "Newmark"
  Newmark Beta = Real 1
  Timestep Intervals(1) = Integer 351
  Timestep Sizes(1) = Real 0.02
  Output Intervals(1) = Integer 1
  Simulation Type = String "Transient"
  Steady State Max Iterations = Integer 20

  Solver Input File = File "laserHeat.laserHeat.sif"
  Output File = File "laserHeat.laserHeat.dat"
  Post File = File "laserHeat.laserHeat.ep"
  Mesh Input File
  File "laserHeat.mif"
End

Constants
  Gravity(4) = Real 0 -1 0 9.82
  Stefan Boltzmann = Real 5.67e-08
End

Body 1
  Name = String "Body1"

  Equation = Integer 1
  Initial Condition = Integer 1
  Material = Integer 1
End

Equation 1
  Name = String "Heat"

  Heat Equation = Logical True
End

Solver 1
  Exec Solver = String "Always"
```

```
Equation = String "Heat Equation"
Variable = String "Temperature"
Variable Dofs = Integer 1
Linear System Solver = String "Iterative"
Linear System Iterative Method = String "BiCGStab"
Linear System Max Iterations = Integer 350
Linear System Convergence Tolerance = Real 1.0e-08
Linear System Abort Not Converged = Logical True
Linear System Preconditioning = String "ILU0"
Linear System Residual Output = Integer 1
Steady State Convergence Tolerance = Real 1.0e-05
Stabilize = Logical True
Nonlinear System Convergence Tolerance = Real 1.0e-05
Nonlinear System Max Iterations = Integer 1
Nonlinear System Newton After Iterations = Integer 3
Nonlinear System Newton After Tolerance = Real 1.0e-02
Nonlinear System Relaxation Factor = Real 1
End

Material 1
  Name = String "glass"

  Density = Real 2530
  Heat Capacity = Real 840
  Heat Conductivity = Real 0.96
End

Initial Condition 1
  Name = String "T0"
  Temperature = Real 300.3
End

Boundary Condition 1
  Name = String "laser"
  Target Boundaries(1) = Integer 1

Heat Flux = Variable Time
Real
  0      0
  0.21  0
  0.22  8.135E4
  1.24  8.135E4
  1.25  0
  7      0
```

```
End
Heat Transfer Coefficient = Real 10
External Temperature = Real 300.3
Radiation = String "Idealized"
Emissivity = Real 0.92
Heat Flux Bc = Logical True
End
```

```
Boundary Condition 2
Name = String "top"
Target Boundaries(1) = Integer 2

Heat Transfer Coefficient = Real 10
External Temperature = Real 300.3
Radiation = String "Idealized"
Emissivity = Real 0.92
Heat Flux Bc = Logical True
End
```

```
Boundary Condition 3
Name = String "sides"
Target Boundaries(1) = Integer 3

Heat Transfer Coefficient = Real 10
External Temperature = Real 300.3
Radiation = String "Idealized"
Emissivity = Real 0.92
Heat Flux Bc = Logical True
End
```

```
Boundary Condition 4
Name = String "bottom"
Target Boundaries(1) = Integer 4

Heat Transfer Coefficient = Real 10
External Temperature = Real 300.3
Radiation = String "Idealized"
Emissivity = Real 0.92
Heat Flux Bc = Logical True
End
!End Of File
```

Bibliography

- [1] Harris C. and Stephens M. A combined corner and edge detector. *ALVEY Vision Conference*, pages 147–151, 1988.
- [2] the Finish IT center for science CSC. Elmer, open source finite element software for multiphysical problems. Available at:<<http://www.csc.fi/english/pages/elmer>>[Accessed June 18, 2008].
- [3] M. Goesele et al. Disco: acquisition of translucent objects. *ACM Trans. Graph.*, 23(3):835–844, 2004.
- [4] O. Morel et al. Active lighting applied to three-dimensional reconstruction of specular metallic surfaces by polarization imaging. *Appl. Opt.*, 45:4062–4068, 2006.
- [5] W. Matusik et al. Acquisition and rendering of transparent and refractive objects. *Eurographics workshop on Rendering*, pages 267–278, 2002.
- [6] R.B. Fisher and D.K. Naidu. A comparison of algorithms for subpixel peak detection. *Advances in Image Processing, Multimedia and Machine Vision*. Springer-Verlag., 1996.
- [7] Cabruja E. Forest J., Salvi J. and Pous C. Laser peak detector for 3d scanners. a fir filter approach. *ICPR*, 2004.
- [8] Python Software Foundation. Python programming language - official website. Available at:<<http://www.python.org/>>[Accessed June 18, 2008].
- [9] The Eclipse Foundation. Eclipse official website. Available at:<<http://www.eclipse.org/>>[Accessed June 18, 2008].
- [10] G. Agronik G.Y. Sirat, F. Paz and K. Wilner. Conoscopic holography. *Proc. SPIE*, 5972, 2005.
- [11] S. Hasinoff and K. Kutulakos. Photo-consistent reconstruction of semitransparent scenes by density-sheet decomposition. *PAMI*, 29(5):870–885, 2007.
- [12] Lienhard J. IV and Lienhard J. V. *A Heat Transfer Textbook*. Cambridge, MA : Phlogiston Press, 2006.

-
- [13] Forest J. New methods for triangulation-based shape acquisition using laser scanners. *University of Girona, PhD. Thesis*, 2004.
- [14] Jiao J. and Wang X. A numerical simulation of machining glass by dual co2 laser beams. *Optics and Laser Technology*, 40:297–301, 2008.
- [15] Lewis J. Laser heating of an optical fiber. *Applied Optics*, 15(5):1304–1306, 1976.
- [16] Bouguet J-Y. and Perona P. 3d photography on your desk. *Proc. of the Int. Conf. on Computer Vision*, 1998.
- [17] K. Kutulakos and E. Steger. A theory of refractive and specular 3d shape by light-path triangulation. *IJCV*, 76(1):13–29, 2008.
- [18] Li L. Li J. and Stott F.H. Comparison of volumetric and surface heating sources in the modeling of laser melting of ceramic materials. *International Journal of Heat and Mass Transfer*, 47:1159–1174, 2004.
- [19] K. Kobayashi M. Fanany, I. Kumazawa. A neural network scheme for transparent surface modelling. *GRAPHITE*, pages 433–437, 2005.
- [20] Konica Minolta. Konica minolta official website. Available at:<<http://www.konicaminolta.com/instruments/products/3d/>>[Accessed June 18, 2008].
- [21] Fagueras O. and Luong Q.-T. *The Geometry of Multiple Images*. MIT Press, Cambridge, 2001.
- [22] Jones E. Oliphant T. and Peterson P. Scientific tools for python. Available at:<<http://www.scipy.org/>>[Accessed June 18, 2008].
- [23] Ciegis R. and Norvaisas S. Mathematical modeling of laser heating of metal. *Litovskii Matematicheskii Sbornik*, 31(4):700–707, 1991.
- [24] Hartley R. and Zisserman A. *Multiple View Geometry in Computer Vision*. Cambridge University Press, 2000.
- [25] Open CASCADE SAS. Salome : The open source integration platform for numerical simulation. Available at:<<http://www.salome-platform.org/>>[Accessed June 18, 2008].
- [26] P. Sturm T. Bonfort and P. Gargallo. General specular surface triangulation. *ACCV*, pages 872–881, 2006.
- [27] Tian W. and Chiu W. Temperature prediction for co2 laser heating of moving glass rods. *Optics and Laser Technology*, 36:131–137, 2004.